

Peder Erik Fischer-Griffiths

Mechanical Responses of Topology and Lattice Optimized Structures in Experiment and Simulation

Bachelor's project in Mechanical Engineering

Supervisor: Stergios Goutianos

May 2021

Peder Erik Fischer-Griffiths

Mechanical Responses of Topology and Lattice Optimized Structures in Experiment and Simulation

Bachelor's project in Mechanical Engineering
Supervisor: Stergios Goutianos
May 2021

Norwegian University of Science and Technology
Faculty of Engineering
Department of Manufacturing and Civil Engineering



NTNU

Kunnskap for en bedre verden

Mechanical Responses of Topology and Lattice Optimized Structures in Experiment and Simulation

Peder Fischer-Griffiths

Oppgavens tittel: Mechanical Responses of Topology and Lattice Optimized Structures in Experiment and Simulation	Dato: 18.05.2021 Antall sider: 66		
	Masteroppgave:	Bacheloroppgave	X
Navn: Peder Erik Fischer-Griffiths			
Veileder: Stergios Goutianos			
Eventuelle eksterne faglige kontakter/ veiledere: NA			

Norsk sammendrag:

Topologioptimering og gitre (lattices) er metoder for å produsere lettvektstrukturer som samtidig kan maksimere (eller minimere) ulike mekaniske egenskaper i forhold til massen. Målet med denne avhandlingen er å undersøke de mekaniske egenskapene til prøver laget med to ulike topologioptimeringsmetoder (SIMP og RAMP) og gitteroptimering for en enkel to dimensjonal trepunkts nedbøying problem. Prøvene ble testet eksperimentelt og simulert med elementmetoden. 14 ulike geometrier har blitt 3D printet og testet. Ti topologioptimerte strukturer ble generert med SIMP og RAMP metoden i Abaqus, med sluttvolumfraksjoner i intervallet 30%-70% for hver 10% steg. Tre gitterstrukturer ble produsert med en Python-kode med utgangspunkt i data fra et topologioptimeringsresultat fra Abaqus. En referansegeometri ble også produsert og testet. Alle prøvene ble utført på en universell testmaskin med trepunkts bøyefester. De topologioptimerte prøvene og referansen ble simulert i Abaqus. Resultatene fra eksperimentene ble brukt til å sammenlikne stivheten, bære-evnen, og arbeid-til-brudd for de ulike geometriene. De eksperimentelle resultatene ble også sammenliknet med simuleringene. Resultatene viser at både topologioptimering og gitterstrukturer har høyere spesifikke egenskaper, i forhold til massen, sammenliknet med referansen, med unntak for enkelte geometrier når det gjelder arbeid-til-brudd. Noen observasjoner fra testingen og generelle problemstillinger knyttet til den praktiske bruken av disse optimeringsmetodene blir diskutert.

English abstract:

Topology optimization and lattice structures are light weighting methods that can maximize (or minimize) different mechanical responses of structures relative to their mass. The aim of this thesis is to study the mechanical properties of sample geometries produced using two different topology optimization methods (SIMP and RAMP) and optimized lattices for a simple two-dimensional mid-point bending problem. Sample geometries were tested experimentally and through finite element analysis. Fourteen different geometries were 3D printed and tested. Ten topology optimized geometries were generated with the SIMP and RAMP methodologies in Abaqus, with volume fractions in the interval between 30%-70% for each 10% step. Three optimized lattices were generated with a Python code utilizing topology optimization results from Abaqus. A reference geometry was also manufactured and tested. All samples were tested on a universal testing machine, using a standard three-point bending fixture. The topology optimized

and reference geometries were simulated in Abaqus. Results from the experiments were used to compare the stiffness, load capacity, and work to fracture of the sample geometries. Experimental results were also compared to the simulations. The results show that both the topology optimized and optimized lattice structures have higher specific mechanical properties, when normalized over mass, than the reference, except for work to fracture for some of the geometries. Some observations from the experiments and general perspectives on the practical application of these optimization methods are discussed.

Stikkord:

Topology Optimization
Lattices
Mechanical properties
Specific stiffness
Specific load capacity
Specific work to fracture



(sign.)

Table of Contents

Table of Contents.....	v
Introduction	1
1.1. Research question.....	2
1.1.1. Operationalization	3
1.2. Theoretical foundations.....	4
1.2.1. Topology optimization	4
1.2.2. General description of topology optimization algorithm	8
1.3. 2D Topology and Lattice Optimization Problem.....	9
1.3.1. 2D problem	10
1.3.2. Topology optimization parameters.....	10
1.3.3. Convergence time	12
1.3.4. Summary of topology optimization processes.....	12
1.3.5. 2D optimized lattices	14
2. Testing and simulation of optimized geometries	23
2.1. Experimental testing.....	23
2.1.1. Samples.....	23
2.1.2. Pre-processing.....	24
2.1.3. Printing.....	25
2.1.4. Storage, conditioning, and preparation of samples.....	25
2.2. Testing of the samples	26
2.2.1. Testing apparatus.....	26
2.2.2. Test setup.....	27
2.2.3. Measurements	27
2.3. Simulation	28
2.3.1. Finite element simulation of geometries.....	28
2.3.2. Simulation setup and execution	28
2.4. Other tools	30
3. Results.....	31
3.1. Experimental results	31
3.1.1. Sample mass analysis.....	31
3.1.2. Results three-point bending: Stiffness.....	32
3.1.3. Results three-point bending: Stiffness.....	36
3.1.4. Results three-point bending: Load capacity	37

3.1.5.	Results three-point bending: Work of fracture	38
3.2.	Results from finite element simulation	40
3.2.1.	Simulation results: Force-displacement graphs.....	41
3.2.2.	Simulation results: Stiffness of SIMP 70, RAMP 70, and reference	42
3.2.3.	Convergence analysis simulation results	43
3.3.	Simulation results and DIC.....	44
3.4.	Failure of topology optimized and lattice structures.....	48
4.	Discussion.....	51
4.1.	Potential applications and further avenues of study for lattice structures.....	51
4.2.	Challenges	51
4.2.1.	Fatigue life of topology and lattice optimized structures.....	51
4.2.2.	Qualification and quality assurance.....	52
4.2.3.	Simulation of lattice structures.....	53
4.2.4.	Topology optimization with manufacturing constraints.....	54
5.	Conclusions	55
6.	References	57
Appendix	59
List of figures.....	59
Project timeline.....	60
Time budget	60

Introduction

Structural optimization has a long history in engineering. Truss structures, I-beams, and hollow tubes are examples of optimization methods that aim to minimize mass, deflection, or compliance in structural applications. Such classical optimization problems can be solved analytically and without the aid of computers. With the rapid expansion of computational resources, significantly more complex optimization methods have been developed and made available. One such method is topology optimization. Topology optimization is an integrated part of many engineering software tools and can be used to create highly complex geometries that would be difficult to find with other means.

Producing the geometries created by topology optimization is often challenging, if not impossible, with traditional manufacturing techniques, such as machining, casting, sheet bending and forming. Digital additive manufacturing technology enables the production of such complex geometries, and as this technology becomes more widespread, advanced optimization can be applied to a larger degree in structural engineering applications.

Another promising optimization and light weighting scheme is the use of lattice structures. Lattices are space-filling cellular structures. They can be both stochastic (Voronoi, branched, or foam-like lattices) or uniform (graph lattices or triply periodic minimal surfaces) (Pan et al. 2020). Replacing solid material with lattice structure can reduce mass. This can be done by shelling a part, i.e. removing interior material, and filling it with lattice structure. Lattice parameters can be manipulated to achieve improved performance. For example, the lattice thickness can be controlled by using a stress field from a finite element analysis, adding material where the stresses are high or removing where they are not. Lattice orientation can also influence its reaction to loading, increasing or decreasing its stiffness. Additive manufacturing has enabled the fabrication of complex lattice geometries.

Combining topology optimization, lattices, and additive manufacturing can produce highly optimized, light weight parts that meet the structural requirements for diverse applications. This technological synthesis can have a significant positive impact on the performance of engineering structures and may also reduce their environmental impact. In many applications, for example transportation or aerospace, mass reduction can decrease energy consumption, increase vehicle performance or payload, and/or increase range (Gay et al.

2003). Additive manufacturing (AM) may also have lower environmental impacts than traditional manufacturing techniques, especially for metallic components. Liu et al. (2018, p.843) present findings that suggest that optimized, AM metallic parts can have life cycle impacts roughly one third of conventional metal parts.

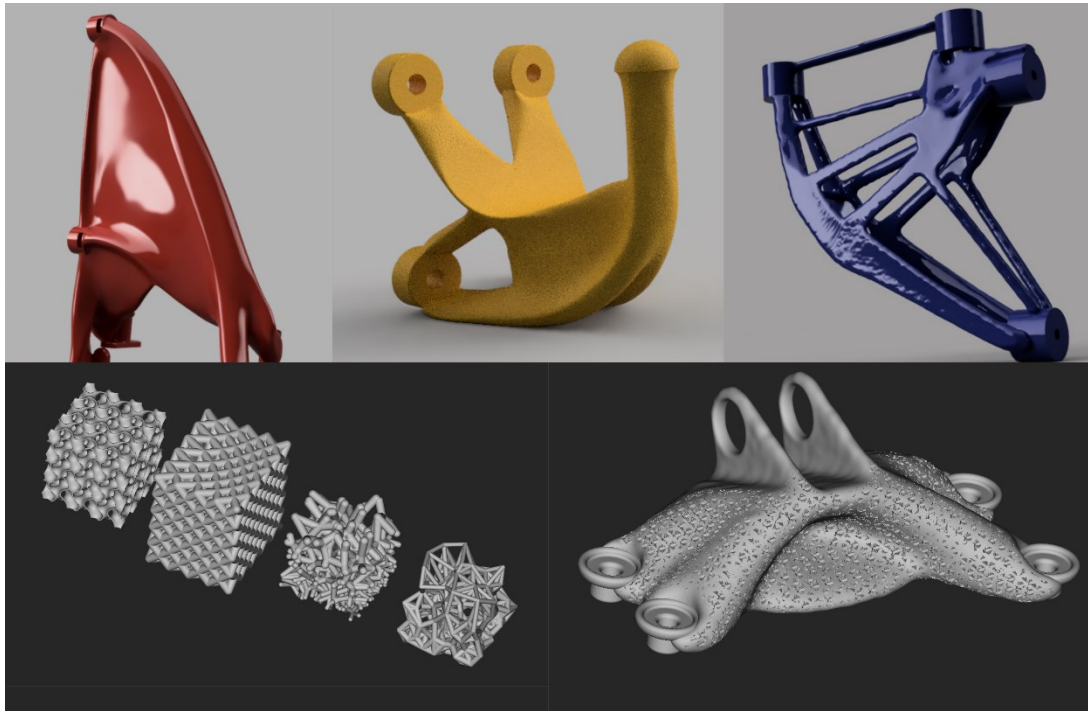


Figure 1: Top row, left to right, examples of topology optimized geometries that have been manufactured, bracket and coat hanger, bracket on far right has not been manufactured. Bottom, left: Examples of lattice structures, from left to right, triply periodic minimal surface (TPMS, gyroid), graph lattice with graded cell size and orientation (octet), stochastic Voronoi lattice (with graded lattice thickness), and a stochastic orthofoam lattice. Bottom, right: Combined topology optimized and lattice structure. (All images author's own work).

1.1. Research question

While topology optimization and lattice structures, combined with AM, seem like promising technologies for the future it seems reasonable to study their structural effectiveness. This thesis aims to investigate, through experiments and simulations, the structural performance of specific solutions to a clearly defined optimization problem using both topology optimization and optimized lattice structures. The main research question is:

- How does the structural performance of topology optimized geometries and optimized lattices compare to that of a reference geometry?

To gain more insight into how changing optimization parameters effects the outcome, a secondary research question has been formulated:

- How are the optimization outcomes effected by the choice of parameters and methods?

1.1.1. Operationalization

The operationalization of this research question will be carried out by defining a simple two-dimensional structural problem that will form the basis for comparison of optimization methods. An initial reference geometry will be the starting point for all optimized geometries, and all geometries must fit within this initial geometry. Restricting the problem to 2D has the benefit of reducing the requirements for computational resources and programming complexity, while also allowing standard testing methods to be utilized. Although the initial problem is 2D, all geometries will be extruded along the out-of-plane normal vector (e.g. the z direction for the xy plane) to create 3D geometries. These 3D geometries will be fabricated and tested using testing apparatus available at NTNU Gjøvik. Simulations of the geometries will also be conducted to compare with, and corroborate, the experimental results.

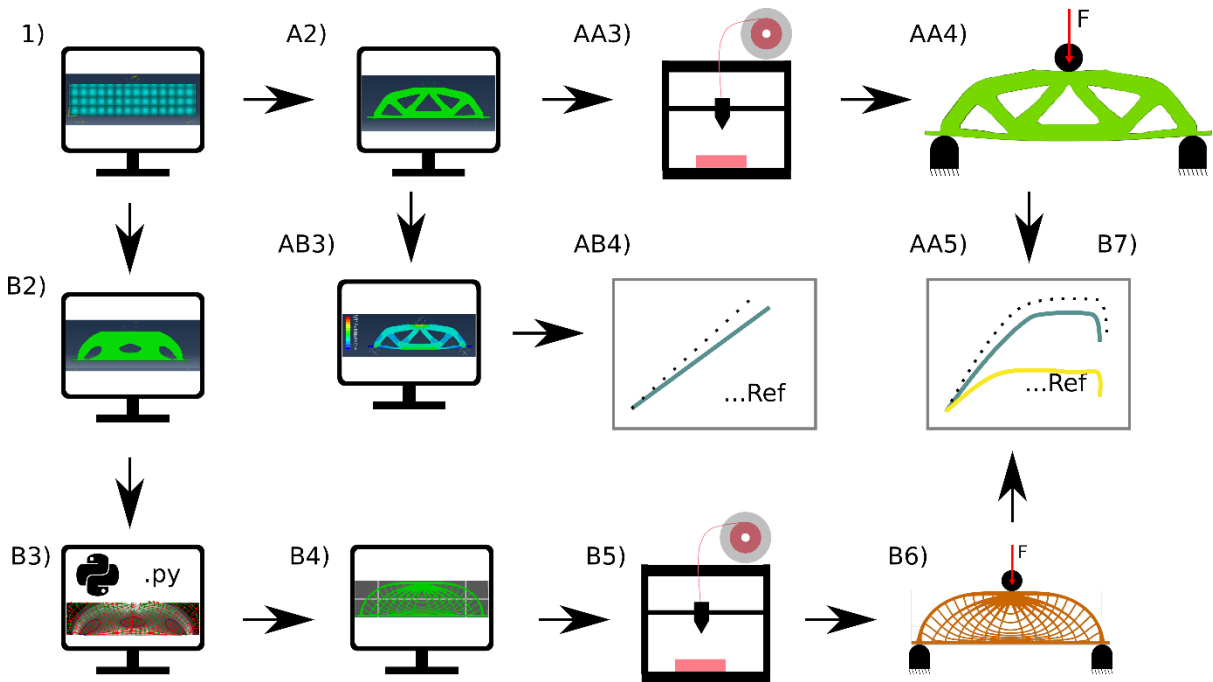


Figure 2: Schematic illustration of project workflow

Fig. 2: Schematic illustration of project workflow		
Step	Description	Section in thesis
1)	Model of initial 2D problem in Abaqus	1.3.

A2)	Topology optimization (TO) in Abaqus	1.2.1.-1.2.2. (theory), 1.3.2.- 1.3.4.
AA3)	3D printing of TO geometry	2.1.2.-2.1.4.
AA4)	3-point bending tests of TO geometry	2.2.
AA5)	Experimental results TO geometry	3.1.
AB3)	Simulation of TO geometry in Abaqus	2.3.
AB4)	Simulation results	3.2.-3.3.
B2)	TO in Abaqus, SIMP method, penalization factor = 1	Table xx, same as A2)
B3)	Creation of lattice geometry in Python using data generated by TO in Abaqus	1.3.5.
B4)	Post-processing of lattice geometry for 3D printing	1.3.5.4.
B5)	3D printing of lattice geometry	Same as AA3)
B6)	3-point bending tests of lattice geometry	Same as AA4)
B7)	Experimental results lattice geometry	Same as AA5)

1.2. Theoretical foundations

1.2.1. Topology optimization

Topology optimization is a mathematical method for finding the optimum distribution of material for a given set of constraints. It is an iterative method that solves the optimization problem on a discretized domain using finite element analysis (FEA). The topology optimization approach studied here is based on the method proposed by Bendsøe & Sigmund (2003). This method is deterministic, in the sense that using the same methods, parameters, and discretization will yield the same results. In contrast to size and shape optimization, where the shape of the design is known in advance, the goal of topology optimization is to find an unknown optimal shape. (Bendsøe 1995, p. 5). A well-formulated optimization problem requires the definition of a specific design space, often called Ω , that is a subset of Euclidean 2D or 3D space. This geometric constraint is necessary to make the set of potential solutions finite. (Stolpe & Svanberg 2001, p. 116). The optimization method seeks a globally optimal solution for this specific design space.

Topology optimization problems are formulated with an objective function that is to be minimized or maximized, e.g. global compliance, strain energy or eigenfrequencies.

Additional conditions are added that constrain the problem, for example a volume or mass fraction of the final topology. The optimal solution to the topology optimization problem is found within the domain of the imposed constraints.

Topology optimization seeks to create a composite consisting of two, or more, materials with different, non-zero elastic properties. One material has very low elastic properties and represents a void, the other represents a specific material, e.g. steel. In its idealized formulation, topology optimization seeks to distribute infinitesimal points of these different materials within the design space. Solving a continuum topology optimization problem is exceedingly difficult, if not impossible, so finite element analysis (FEA) is used as a solution method. In FEA, the design space is discretized and a material property between 0 and 1 is attributed to each element, with 0 representing a void, 1 material, and intermediary values a combination of the properties of the two materials. The ascription of values to the elements is often called the element density function. (Stolpe & Svanberg 2001).

Since creating continuous, isotropic materials with graded elastic properties is problematic, topology optimization methods attempt to assign either a value of 0 or 1 to all elements in the design space. Different methods exist for penalizing intermediary density values for elements. In this thesis two approaches are used and tested, the Solid Isotropic Material with Penalization (SIMP) and the Rational Approximation of Material Properties (RAMP) methods. SIMP and RAMP are interpolation schemes that penalize intermediary values of the density function.

The SIMP method uses a power law, where the elastic property of element j is given by:

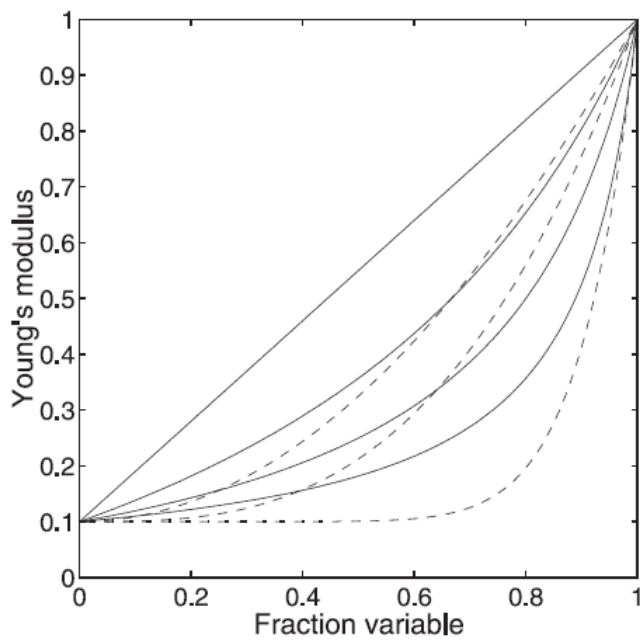
$$E_p(x_j) = E_0 + x_j^p \Delta E$$

Where E_p is the elastic property (Young's modulus) of element j , E_0 is the elastic property of the void material, x_j is the density function of element j and $\Delta E = E_1 - E_0$. Since $x_j \in (0,1]$, choosing values for $p > 1$ will reduce the stiffness achieved for material fraction used for intermediary values of the density function. (Stolpe & Svanberg 2001, p.119)

Stolpe & Svanberg (2001) suggest an alternative method for interpolation that has become known as RAMP. The elastic property of element j is given by:

$$E_q(x_j) = E_0 + \frac{x_j}{1 + q(1 - x_j)} \Delta E$$

Choosing values for $q > 0$ will also penalize intermediary values of the density function. (Stolpe & Svanberg 2001).



A comparison of the SIMP model and the alternative model when $E_1 = 1$ and $E_0 = 0.1$. $E_p(x_j)$ for $p = 2, 3, 10$ are shown as dashed lines; $E_q(x_j)$ for $q = 0, 1.5, 4, 9$ are shown as solid lines

Figure 3: Effect of SIMP and RAMP interpolation on Young's modulus for a given element fraction

Figure 3 (Stolpe & Svanberg 2001, p.119) shows the effect on the Young's modulus of an element with intermediary values for the density function for different values of p and q . The geometries created and tested in this thesis have used values of 1, 2, and 3 for both the SIMP and RAMP methods. Only optimized geometries created with $p=q=3$ have been tested experimentally. Lattice geometry has been created using topology optimization results from SIMP with $p=1$.

In figures 4 and 5 the distribution of element densities from the topology optimization processes in Abaqus for the SIMP method with penalization parameters of 3 and 1 are plotted. For the geometries created using $p=3$, we can see that the fraction of elements with a density value of 1 are highest for the 70% volume fraction and decrease with smaller fractions.

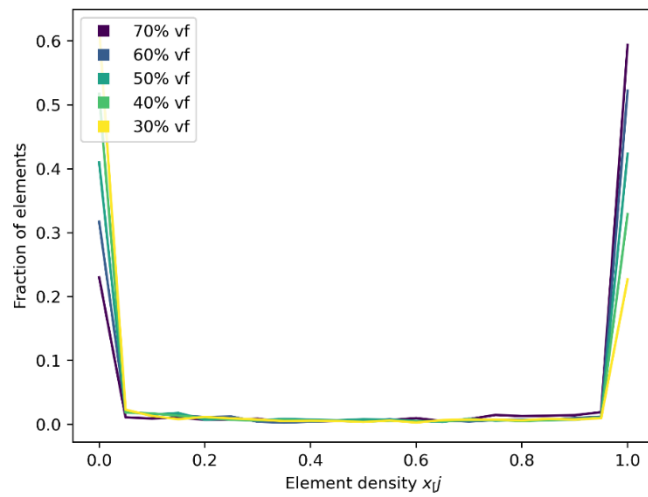


Figure 4: Fraction of elements with element density x_j for SIMP method with penalization factor of 3.

With a penalization factor of 1, the element densities are more varied, with the weight of elements shifting towards higher densities for higher volume fractions. The data for these plots has been generated by Abaqus during the topology optimization processes studied in this thesis.

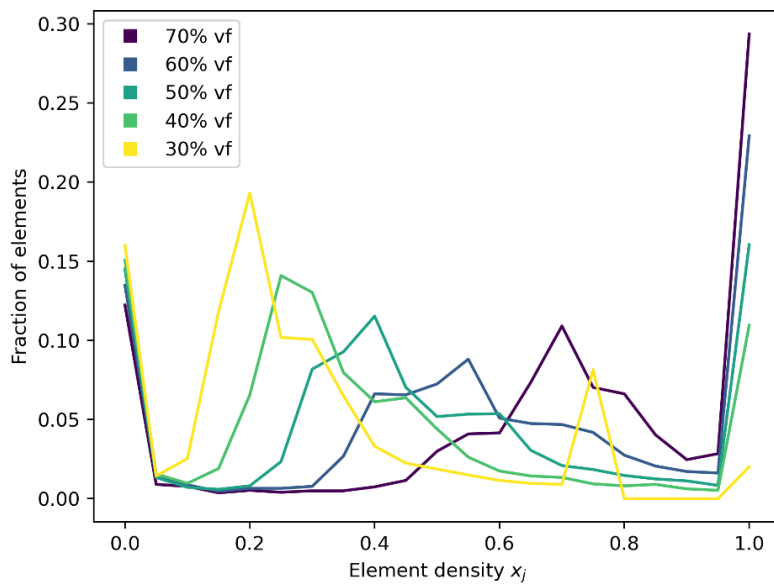


Figure 5: Fraction of elements with element density x_j for SIMP method with penalization factor of 1.

1.2.2. General description of topology optimization algorithm

Software implementations of topology optimization algorithms generally follow the same solution strategy. Different optimization strategies and parameters are available across software platforms, lending varying degrees of control over the optimization process.

1.2.2.1. *Step 1: Definition of design space (Ω) and boundary conditions*

Topology optimization starts by defining a design space (Ω). This design space can include holes or obstacles, i.e. regions where there cannot be material, as well as areas where material is enforced, for example to allow contact with other components. The design space can be represented in many ways - CAD models, meshes, point lists etc.

The boundary conditions for the problem are required to find a solution. Mechanical loads, displacements, thermal loads, or other forces acting on the component must be defined. There can be single loads, multiple loads, or multiple load cases, where different loads act on the structure independently of each other. The design space must be constrained from rigid body movement in at least one point.

1.2.2.2. *Step 2: Discretization of design space*

Topology optimization requires the design space to be discretized. This is usually achieved with finite elements. Elements should be relatively small to reduce the influence they have on the result. Mesh types can also influence the results of topology optimization, especially large triangular elements for 2D problems, where such elements give the material unrealistic stiffness. (Full Integration 2019).

1.2.2.3. *Step 3: Initialization*

The SIMP and RAMP optimization processes usually begin by setting all elements to the constraining value defined in the problem formulation, for example all elements are given a density of 0.5 if the final volume fraction is 0.5. The material properties of the discretized geometry are adjusted accordingly. For example, reducing the volume fraction to 0.5 would reduce the stiffness of the material accordingly, or actually more when using the SIMP and RAMP interpolation schemes. A finite element analysis is then conducted on the discretized geometry with the altered properties.

Depending on what the objective function is, the properties of each element are updated based on the results of the finite element analysis. For example, elements that experience high stresses have material added, while elements with low stresses can have material

removed. The material properties of each element are then updated, and a new finite element analysis is conducted.

1.2.2.4. *Post-processing of topology optimization results*

Since the algorithm calculates a density value for every element in the design space, the solution has the same resolution and edge shape as the discretized mesh. This means that quadrilateral meshes will have 'pixelized' edges in the raw data in 2D, while 3D tetrahedral meshes have faceted faces. In Abaqus, topology optimization results are shown with smooth edges, and exported geometry has been smoothed as well. Filtering and smoothing are common postprocessing techniques to remove mesh-induced geometric irregularities. The geometry reviewed in this thesis has used the default smoothing and filter settings in Abaqus.

1.2.2.5. *Additional methods: Gradient-based and condition-based optimization*

Some algorithms track the change of the global structural performance, according to the objective function, in relation to the change in element density after designated number of iterations. Based on this gradient, a differentiable approximation to the initial problem can be found. Gradient based optimization can be significantly faster. Several methods are suggested in the literature, e.g. Svanberg (1987) or Zhou & Saitou (2018). Abaqus does not include such a gradient based approach but does have an optimization algorithm called condition based. This algorithm does not calculate the local stiffness and is therefore faster, but has more limited capabilities (*About structural optimization*, n.d.). In this thesis, only the density-based algorithms based on Bendsøe & Sigmund (2003) are used. This method does not employ gradients, nor is it condition based.

1.3. 2D Topology and Lattice Optimization Problem

A two-dimensional problem is defined to test topology and lattice optimization methodologies. This is a three-point bending problem that replicates the load and boundary conditions encountered using an Instron 5966 Universal testing machine with a 3-point bending fixture. The reason for choosing this setup is that the optimized geometry in 2D can be extruded to make 3D objects that can be tested, allowing comparison of modelling and testing results.

1.3.1. 2D problem

The initial design space is an 80 [mm] by 20 [mm] planar area. The planar area is supported at both ends by semicircular rigid bodies with a radius of 5 [mm], representing the supports of the 3-point bending fixture. A span length of 70 [mm] is used. Loading is introduced at the midpoint of the top edge by a rigid semi-circular body. A fixed displacement of 1 [mm] is applied to this body. All contacts between support and loading bodies are 'hard contact'.

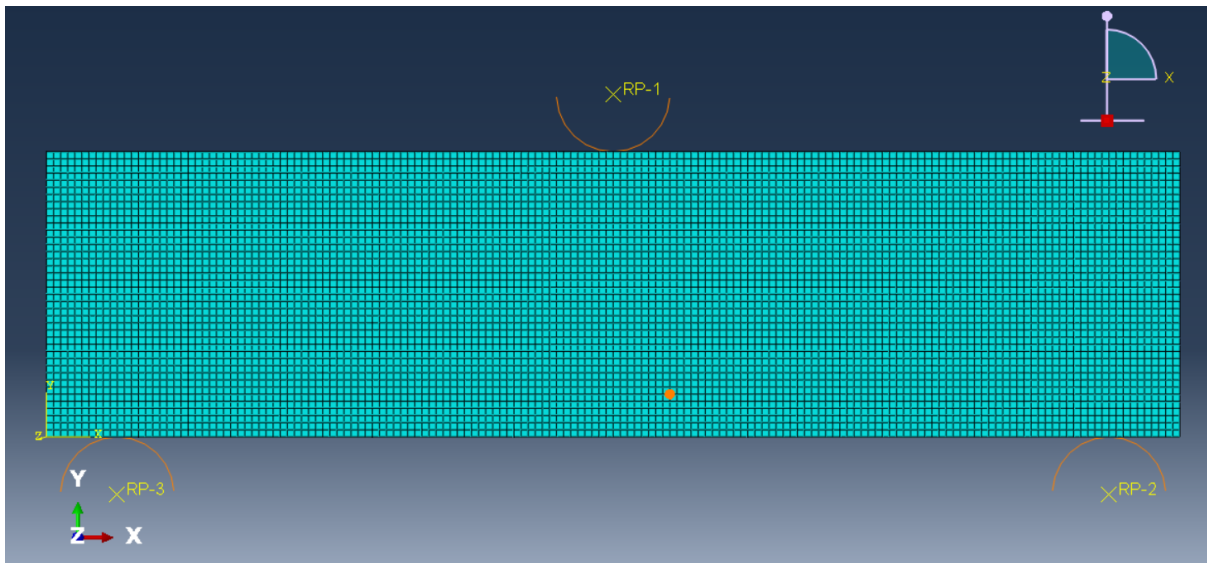


Figure 6: Problem domain. An 80x20 mm² planar area, supported by semi-circular rigid bodies, load applied by semi-circular rigid body. The quadrilateral mesh is shown.

A quadrangular mesh, with edge lengths of 0.5 (mm), is used to discretize the planar area. Quadrilateral elements are used instead of triangular, as triangular meshes can give the discretized body an artificially high stiffness.

1.3.2. Topology optimization parameters

A series of optimization processes were run on the same geometry, each with different parameters. Different combinations of optimization method, final volume fraction, penalization parameter, and final maximum material density were tested systematically. Since the only loading was a prescribed displacement, the optimization process sought to minimize the energy stiffness measure of all elements, under the constraint of a prescribed volume fraction. The energy stiffness measure is calculated by:

$$\frac{P \cdot u}{2} - \frac{R \cdot u^*}{2}$$

where P is the external loading, u are the corresponding nodal deflections, u^* are the prescribed nodal displacements, and R are the nodal reaction forces. (*Design responses*, n.d.). Given that $P=0$, and that $R<0$, minimizing R entails finding the largest possible negative value for R within the problem constraints. If u^* is a fixed value, then R must be as large as possible to minimize the energy stiffness measure.

Geometries with volume fractions ranging from 0.7 to 0.3 (70-30%), in increments of 0.1 (10%) were created. Both SIMP and RAMP strategies were tested at all the volume fraction steps.

Abaqus allows the user to specify the penalization parameter. Penalization values of 1, 2, and 3 were used to create geometries. Early in the optimization trials, it became apparent that some of the geometries displayed poor properties, such as discontinuous material domains. These geometries came from using intermediary values, greater than 1 and less than 3, for the penalization parameter. Only a few optimization runs were carried out with such intermediary values for the penalization parameter. Only geometries with penalization parameter values of 1 and 3 were created for all volume fractions. As mentioned earlier, a penalization parameter of 1 with the SIMP method results in the non-penalization of intermediary values for the density function. For the RAMP method, setting the penalization factor to zero should have the same effect, but these optimization runs would fail in Abaqus. For these reasons, the RAMP method was only tested with intermediary penalization factors for some of the volume fractions.

Abaqus allows the user to specify the desired range of end densities for the elements, from minimum to maximum. In the tests run, a combination of a penalization value of 1 with an end density interval of (0,0.75) was used as the basis for creating lattice structures.

All the other optimization parameters – convergence criteria, maximum number of iterations, etc. – were kept at the default values. This may have affected the results of some of the optimization processes to some extent since this limit was reached in three cases. In only one of these cases was the geometry included in the experiments. Judging from the output files, the energy stiffness measure only changed by 1.17% in the last five iterations.

1.3.2.1. Material properties for topology optimization

Only elastic and density properties of the material were specified in the topology optimization setup. When the optimized geometries were being calculated it was not known what material the samples were going to be 3D printed in. For the elastic properties, a Young's modulus of 210 [GPa] and a Poisson's ratio of 0.3 was defined. A dummy density value of 1.0 [g/cm³] was used.

1.3.3. Convergence time

The number of iterations in the optimization process varied between methods, parameter settings, and volume fractions. This gives some indication of the computational difficulty of the optimization problem for the given settings, but comparing computational requirements based on this measure will have limited reliability, as it is unknown to what extent each iteration is computationally equivalent.

1.3.4. Summary of topology optimization processes

Table 1 and 2 summarize the optimization processes that have been run. The geometry that has been tested experimentally, and that has been used for lattice generation, is indicated. To confirm if the default optimization method in Abaqus is SIMP, runs using both the default and SIMP were conducted. With all parameter settings equal, the default and SIMP method converged in the same number of iterations and produced the same geometry.

Volume fraction	Penalization factor	Iterations	Tested Experimentally	Used for lattice generation	Comments
0.70	3	38	Yes	-	Default
		42	No	-	Min. density set to 0.001, longer convergence time
	2	23	No	-	
	1	21	No	-	
0.60	3	34	No	-	Default method
		45	No	-	Starting density set to 0.75, longer convergence time
		34	Yes	-	SIMP method
	2	50 (max)	No	-	

	1	27	No	-	Starting density 75%
		18	No	-	Starting density 75%, final density 0.1-75%
		18	No	-	
0.50	3	47	Yes	-	
	2	50 (max)	No	-	
	1	17	No	-	
		16	No	-	Final density 1-75%
0.40	3	35	Yes	-	
	2	48	No	-	Geometry errors
	1	16	No	-	
		17	Yes	Yes	Final density 1-75%
0.30	3	32	Yes	-	
	1	17	No	-	Final density 1-75%

Table 2: Summary of topology optimization processes tested with RAMP method					
Volume fraction	Penalization factor	Iterations	Tested Experimentally	Used for lattice generation	Comments
0.70	3	38	Yes	-	
	2	36	No	-	
	1	24	No	-	
0.60	3	37	Yes	-	
	2	41	No	-	
	1	50 (max)	No	-	
0.50	3	41	Yes	-	
0.50 cont.	2	41	No	-	
	1	46	No	-	Geometry errors
0.40	3	43	Yes	-	
0.30	3	50 (max)	Yes	-	

1.3.5. 2D optimized lattices

Intermediary values of the density function indicate that the elastic modulus, and mass, for an element were a fraction of the full value. In practice it is difficult to create a homogenous isotropic material with graded elasticity and mass. It is possible to create an anisotropic material, in this case a lattice structure consisting of homogenous unit cells, that has variable elasticity and mass by manipulating parameters of each unit cell. With additive manufacturing technology, such as Fused Filament Forming (FFF), it is also possible to realize such structures in practice.

In this thesis, lattice optimization using a basic 2D unit cell consisting of a hollow square (see figure 7) will be explored. Parameters that could be used to manipulate the elasticity (stiffness) and material density of the unit cell are: cell size, wall thickness, skewing, and orientation of the cell. Figure 7 shows a representation of the unit cell used in the lattice geometry in this thesis (left) and its elastic properties (right).

Wu et al. (2021) have proposed a method for lattice optimization where the cell orientation, size and skewing are the optimization parameters. Using homogenization to create an elasticity tensor for an anisotropic 2D unit cell, Wu et al. (ibid.) developed a topology optimization finite element code that manipulated the elastic properties of each element by altering the values for the side length and orientation angle. Wu et al (Ibid.) aligned the unit cells with the principal stress directions σ_1 and σ_2 , citing Pedersen (1989) who posits that this orientation is optimal.

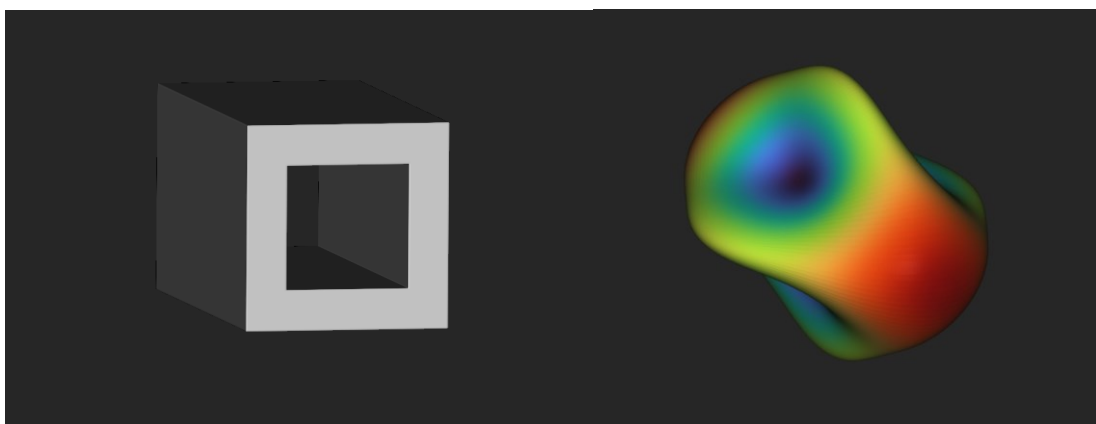


Figure 7: (Left) shows the basic 2D unit cell, extruded to a 3D shape. This is the unit cell used in the lattice geometry in this thesis, as well as by Wu et al. (2021). (Right) is a representation of the 3D elastic properties of the unit cell on the left. Red indicates higher stiffness, green intermediary, and blue lower.

Allowing the unit cells to align with the principal stress directions should give the entire lattice structure higher stiffness and strength. Looking at figure 6 (right) we can see that the unit cell is stiffer in the in-plane direction parallel with the walls than diagonally across the corners. A force working diagonally across the cell leads to bending dominated deformation of the unit cell, while a force working parallel to the walls leads to predominantly axial deformation, which the unit cell is more able to resist. Shear forces parallel to the cell walls cause diagonally oriented deformation of the cell. If the unit cell is locally oriented along the principal stress directions, the shear forces will, in theory, be zero. All forces acting on the cell will then be axial, thereby loading the cell in its strongest direction. Figure 8 shows the Mohr's circle interpretation of a 2D stress state in a solid isotropic material. The maximum principal (σ_1) and minimum principal (σ_2) stresses are found on a line where the shear stress (τ_{12}) components are zero. Rotating the unit cell by θ brings the cell walls in alignment with the principal stress direction.

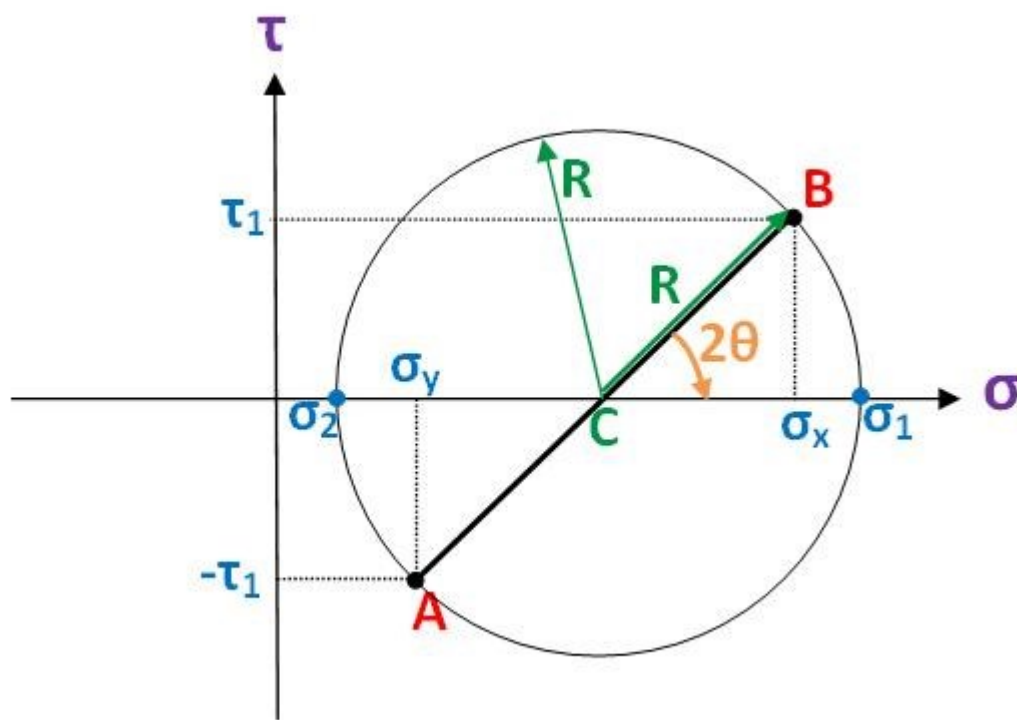


Figure 8: Mohr's circle representation of 2D stress state. (Source: https://commons.wikimedia.org/wiki/File:Mohr_diag17.JPG, accessed 12.04.2021, author Taltastic)

The topology optimization results in Abaqus include stress data (σ_{11} , σ_{22} , σ_{33} , and σ_{12}) for every element centroid. It is also possible to extract the principal stress data directly from

Abaqus, but these values were calculated using Python. Since this is a 2D plane strain problem the s_{33} values all equaled 0. σ_1 and σ_2 values were calculated for all element centroids in the design space. The angle between the global coordinate system (x,y,z) and the principal stress direction in a material point is 2θ , see figure 8. Finding the angle θ is done by:

$$\theta = \frac{1}{2} \arctan\left(\frac{2\sigma_{12}}{\sigma_{11} - \sigma_{22}}\right)$$

Using the arctan function is problematic in this application since the function values are only in the interval $\left[-\frac{\pi}{2}, \frac{\pi}{2}\right]$. This could end up rotating the actual angle θ by π radians and would require additional steps to mitigate. The Numpy *atan2* function was used instead as its function values are in the interval $[-\pi, \pi]$. It calculates the angle with the basis vector $\vec{e}_1 = [1,0]$. Using the atan2 function provided correct results for the angle θ .

Inserting the θ value in the following formula defines a discrete vector field for all element centroids consisting of unit vectors expressed in the global coordinate system.

$$\mathbf{F}_{\sigma_1} = \begin{bmatrix} r \cdot \cos(\theta) \\ r \cdot \sin(\theta) \end{bmatrix}$$

Where \mathbf{F} is a discrete vector field. Setting r to 1 provides unit vector components in the global x and y direction for all element centroids in the discrete vector field. This approach yielded a discrete vector field for σ_1 .

The discrete vector field for σ_2 was found by relying on the fact that σ_2 is perpendicular to σ_1 in all points. In \mathbb{R}^2 this can be done with the following formula:

$$\mathbf{F}_{\sigma_2} = \begin{bmatrix} -r \cdot \sin(\theta) \\ r \cdot \cos(\theta) \end{bmatrix}$$

Again, setting r to 1 yields discrete unit vector components for σ_2 in the global x and y directions for all element centroids.

1.3.5.1. Methodology for generating lattice geometry in Python

A Python code has been written to generate the lattice geometry studied in this thesis. Due to time constraints, a basic approach was implemented. The basis for the lattice geometry

was two sets of lines, one for each of the principal stress fields, plus additional lines along the boundaries. These lines were found by following the discrete vector fields from a set of starting positions, using a numerical method. See table 3 for starting points used to generate the lattices. In general form, the scheme for finding the next point p_{i+1} is:

$$p_{i+1} = p_i + s \cdot \mathbf{F}(p_i)$$

Where p_i is the position at the previous step, s is the step size (chosen to be 0.25 mm) and $\mathbf{F}(p_i)$ is the unit vector at point p_i found from the discrete vector field for σ_1 or σ_2 . Since the vector field F is not defined for every point of space in Ω , the unit vector in F that is closest to point p_i is used. Starting from an initial point p_0 new points were found until an end condition was met. As the problem is symmetric, only half of the design space Ω was filled with lines, and the stop conditions for line generation were $x=40.25$ and $y=20$.

Line group	Starting points (x,y)
σ_{\min} (compressive) stress field	(5,0), (10,0), (15,0), (20,0), (25,0), (30,0), (35,0), (40,0)
σ_{\max} (tensile) stress field	Points for this line were seeded along the σ_{\min} line starting from (5,0) with 3.75 mm spacing along the curvature. Initially 5mm spacing was used but was later reduced.

Table 3: Starting points for lattice generation

Since the fields F_{σ_1} and F_{σ_2} are perpendicular to each other in every point, the set of lines described above was used to create a grid of unit cells when merged. Figure 8 illustrates the stream plot for the design space. It also shows the material density contours from the topology optimization. The data represented by this image are used to generate the lattice geometries.

One disadvantage with the chosen methodology is that the cell size changed throughout the geometry. Only at the initial positions are the cell size dimensions correct. This reduces the validity of the comparison with the unoptimized lattice geometry, which has uniform cell

size throughout.

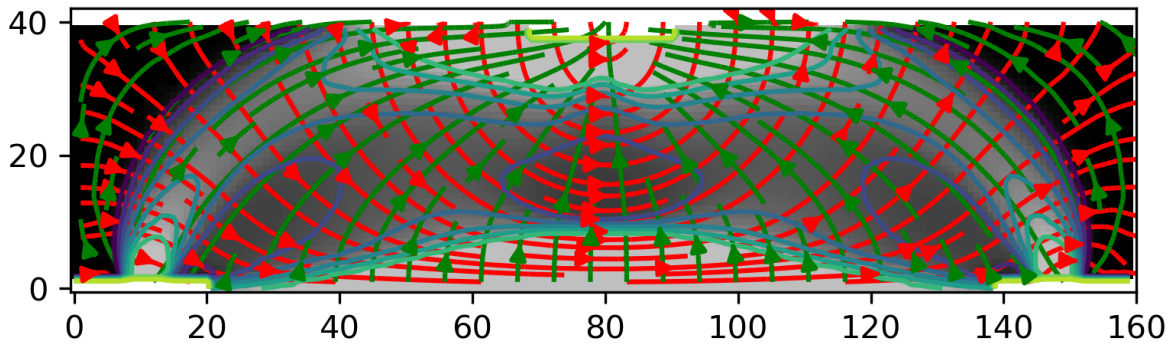


Figure 9: Co-projection of stream plot for principal stress fields and density function. Red lines indicate the σ_1 (tensile) field, while the green lines are the σ_2 (compressive) field. The contour lines, shaded purple to light green, are for the values of the density function, a scalar field. The grey scale image in the background is a representation of the density function scalar field.

1.3.5.1.1. Brief comment on the stress fields

In this specific problem the stress fields discussed above were purely tensile (σ_1) and purely compressive (σ_2). Other geometries and loading conditions can lead to compressive stresses in the S_1 field and visa versa.

1.3.5.2. Wall thickness of optimized lattices

Wu et al. (2021) used a constant wall thickness for easier manufacturing. The lattices geometries reviewed in this thesis used constantly varying wall thicknesses. Wall thickness was driven by data generated from the topology optimization. The line sets described in the previous section can represent the center path between adjacent unit cells. On either side of these lines, a wall thickness was added. Since the initial unit cell was 5×5 [mm]², the maximum wall thickness on either side is $5/2 = 2.5$ [mm]. Wall thickness of the lattice was generated using the magnitude of the principal stress in point p_i to set the distance from the center path.

$$\hat{p}_i = p_i + \frac{\sigma(p_i)}{\sigma_{max}} \cdot 2.5 \cdot F_s(p_i)$$

Where \hat{p}_i is the point designating the wall thickness, $\sigma(p_i)$ is the principal stress magnitude in point p_i , σ_{max} is the maximum principal stress in the design space, and F_s is the unit vector field value in point p_i for the perpendicular principal stress direction. This method was the one used for producing lattice geometry. Three modifications of the ratio σ/σ_{max} were used to create lattice geometry that was tested. For the geometry called 'Lattice 1', σ_{max} for the principal stress σ_1 (tensile) was set to the maximum value of σ_1 , and for the σ_2 lines, σ_{max}

was set to the minimum (largest absolute) value of σ_2 . Since the largest value for σ_1 was around 37 and the largest value for σ_2 was around 257, the wall thickness of the tensile members was relatively greater compared to the compressive members. A second geometry, called 'Lattice 2' was made with an alteration to the σ_{max} value. In this configuration σ_{max} was set to the highest overall value (σ_2) for both tensile and compressive members of the lattice. With this modification, the wall thickness of the tensile members was greatly reduced, but the compressive members were still relatively thin. Another modification was made to the wall thickness function. The ratio σ/σ_{max} was altered to:

$$\left(\frac{\sigma(p_i)}{\sigma_{max}}\right)^{\frac{1}{2}}$$

Raising this ratio to the power of 0.5 increased the value of ratio between 0 and 1, adding more thickness to the walls in the compressive principal stress direction.

The geometry called 'Lattice 3' was similar to 'Lattice 2' but changed the power of the σ/σ_{max} ratio to $\frac{1}{3}$, increasing the intermediary values of the wall thickness further.

Figure 10 presents a schematic illustration of the lattice generation process.

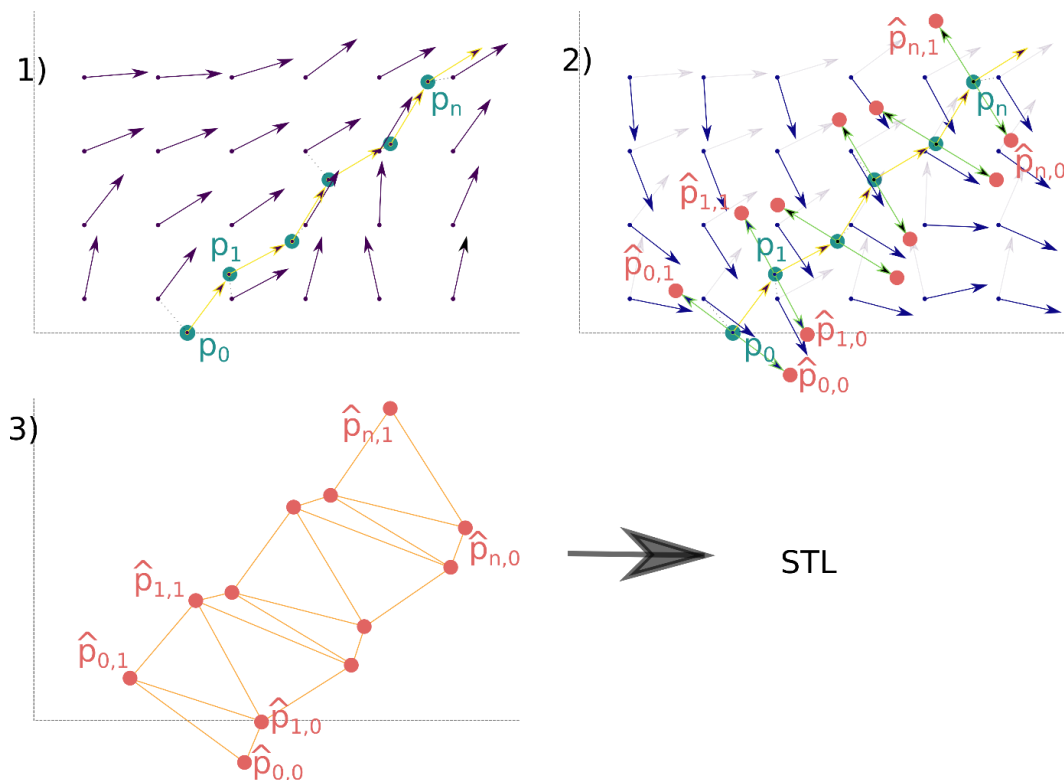


Figure 10: Schematic of the lattice generation process. In 1) a set of points (representing a line) following the unit vector field for one of the principal stresses is defined. In 2) points are defined on either side of the line from 1). The unit vector

field for the other principal stress controls their direction, and the magnitude of the principal stress in point p_i determines the distance from point p_i . In 3) the points are triangulated. A list of points (a $n \times 3$ matrix) and a list of connections (a $m \times 3$ matrix) is used to generate an STL file. The grey dashed line represents the valid area for geometry. In post-processing, parts of the geometry that were outside this area were trimmed. The process is shown in 2D here, while the resulting geometry is 3D.

1.3.5.3. Modification for FFF/FDM 3D printing: Minimum wall thickness

Figure 11 (left) shows a CAD geometry representing different wall thicknesses. From left to right the wall thicknesses are [0.50, 0.45, 0.35, 0.25] [mm]. On the right in figure 10 is the interpretation of this CAD geometry by the slicer software that generates G-code for the printer. Even with the nozzle diameter set to 0.20 mm, only the 0.50 mm wall thickness is produced. Wall thicknesses less than 0.50 mm must be avoided if the geometry is to be produced using the printers available at NTNU, Gjøvik. In the Python code that generates the lattice geometry, a basic approach was implemented. Any wall thinner than 0.25 mm was given a thickness of 0.25 mm. Since the code generated a wall thickness on either side of the center line, this produced a wall thickness of 0.5mm in the final part.

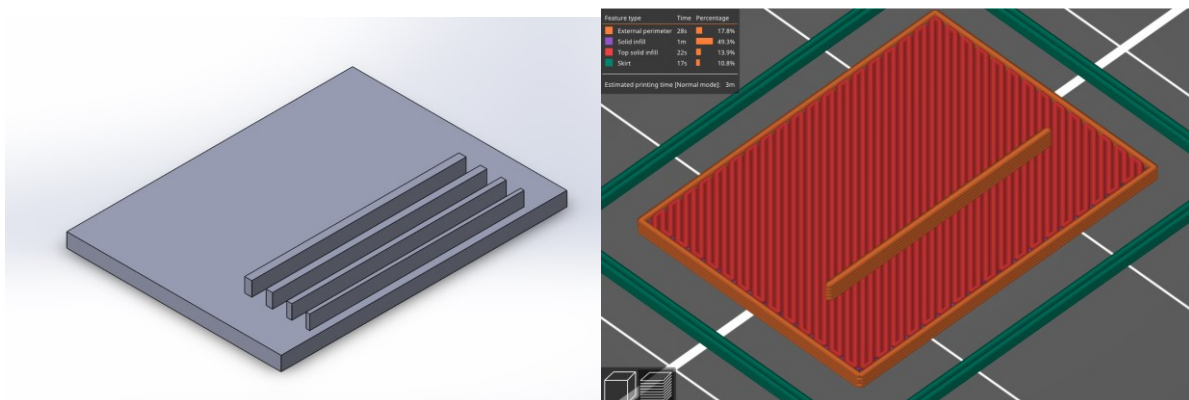


Figure 11: CAD geometry and its interpretation by 3D printing slicer software.

1.3.5.4. Post-processing and printing of lattice geometry

After the points designating the wall thickness were generated in the Python code, a connectivity list representing edges in triangles was created. Using a module called numpy-stl 2.16.0 (Hattem ND), STL files were generated based on the list of points and connectivity list. An STL file was exported from the Python script and post-processed using the PrusaSlicer software. First the STL files were repaired using the built-in function. Second, since only half of the geometry was created in the Python code, it was mirrored to create the final lattice structure. The lattice structures were then sliced and printed using the same settings, printers, and material as the topology optimized samples. Figure 12 shows the three different tested lattice geometries.

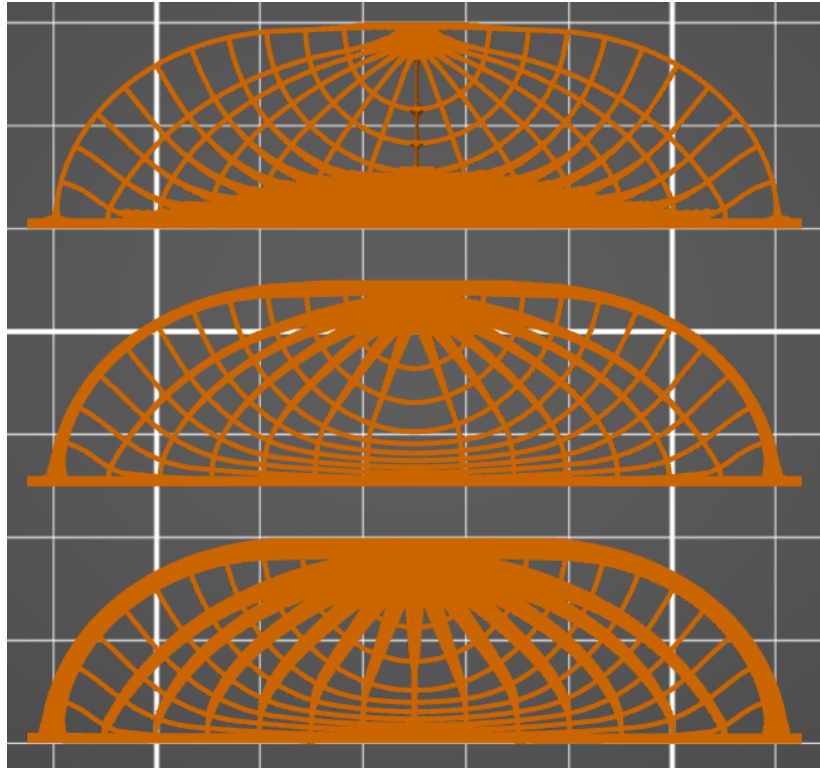


Figure 12: The three generated lattices. From top to bottom: Lattice 1, Lattice 2, Lattice 3.

2. Testing and simulation of optimized geometries

Topology and lattice optimized geometries, along with reference geometries, were manufactured and tested. The topology optimized and reference geometries were also simulated in Abaqus using finite element analysis. In this section/chapter the experimental and simulation process will be reviewed in detail. Starting with the production process, continuing with the experimental setup, and finishing with the simulation process.

2.1. Experimental testing

2.1.1. Samples

A total of 14 different geometries were manufactured and tested. Five sample groups with 0.70, 0.60, 0.50, 0.40, and 0.30 volume fractions were produced with both the SIMP and RAMP topology optimization methods. Three optimized and two reference lattice geometries were produced. The reference lattice geometry consisted of the same unit cell on a rectangular grid with cell edges parallel to the main axis directions. Reference samples, representing the initial three-point bending problem, were fabricated. Each sample group had

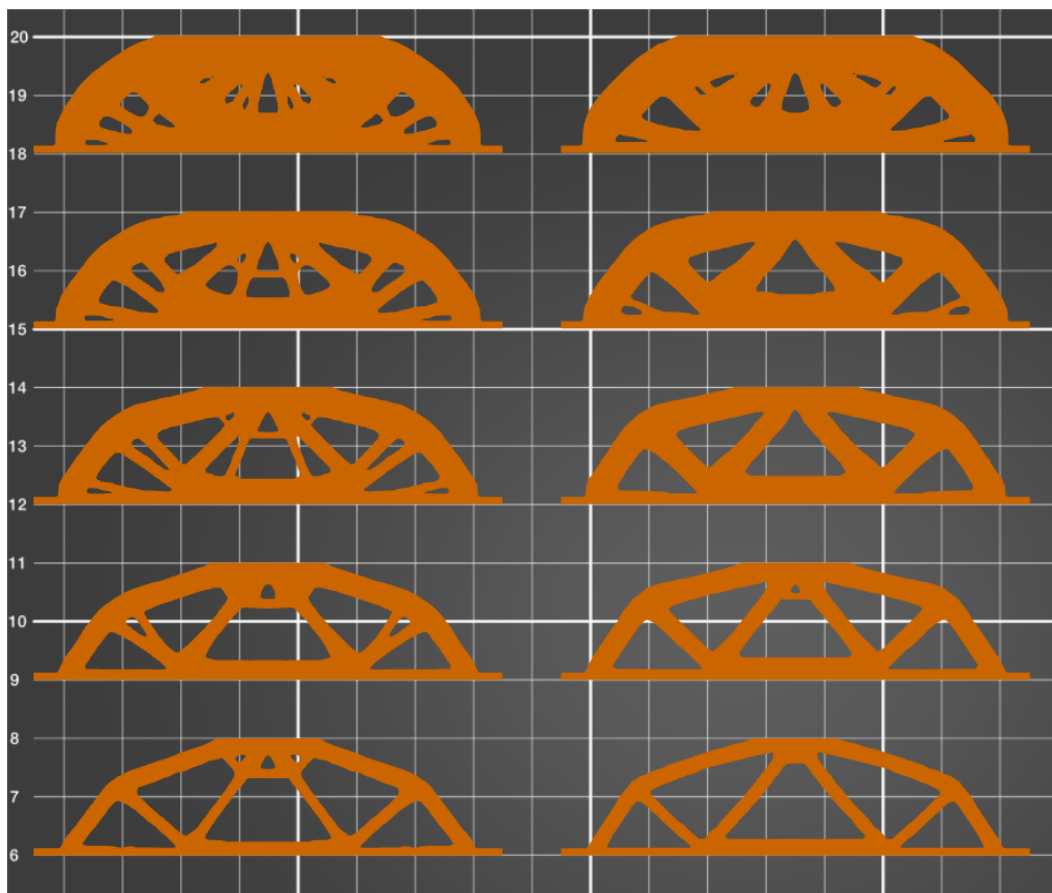


Figure 13: Tested topology optimized geometries. SIMP on the left and RAMP on the right. From top in descending order by volume fraction.

two

samples. Table 4 summarizes the sample groups. Figure 13 shows the topology optimized geometries.

Optimization method	Volume Fraction				
	0.70 (70%)	0.60 (60%)	0.50 (50%)	0.40 (40%)	0.30 (30%)
SIMP	SIMP7001	SIMP6001	SIMP5001	SIMP4001	SIMP3001
	SIMP7002	SIMP6002	SIMP5002	SIMP4002	SIMP3002
RAMP	RAMP7001	RAMP6001	RAMP5001	RAMP4001	RAMP3001
	RAMP7002	RAMP6002	RAMP5002	RAMP4002	RAMP3002
Lattices	Lattice 1	Lattice 2	Lattice 3		
	LE1_1	LE2_1	LE3_1		
	LE1_2	LE2_2	LE3_2		
Reference (original geometry)	REF1				
	REF2				

Table 4: Manufactured and tested samples.

2.1.2. Pre-processing

All samples were manufactured using fused filament forming (FFF)/fused deposition modeling (FDM) additive manufacturing method. STL files of the geometries were processed using PrusaSlicer V2.3.0 for Windows 64. Layer height was set to 0.20 mm. A standard material preset, Generic PLA, in the slicer was used. The default present 0.20 mm QUALITY was used in the PrusaSlicer. ‘Quality’ in the setting name refers to the print speed and acceleration being lower than for the ‘SPEED’ standard setting. Print times are longer with this setting, but print resolution, details, tolerances, and quality are higher. Two modifications were made to the ‘QUALITY’ setting. Infill density was changed to 100% and infill pattern, by necessity, was changed to rectilinear. The standard infill for the ‘QUALITY’ setting is gyroid, but at 100% infill this pattern cannot be printed on Prusa printers with the standard settings. Rectilinear infill is the default for 100% dense prints, and this was the reason for accepting this setting. A summary of the most important settings is provided in table 5. The Prusa Mk3 was selected as the printer in the software. No other modifications

to the standard settings were made. After configuring the print settings, the objects were sliced, and the G-code file was exported to a SD-card.

Printer setting	Value
Bed temperature	60°C
Nozzle temperature	215°C (first layer)/210°C (remainder)
Perimeters	2
Support material	None
Print speeds	Peri.:45mm/s, small peri.:25mm/s, ext.peri.:25mm/s, infill: 80mm/s
Cooling	Fan always on, auto cooling enabled
Nozzle diameter	0.4mm
Infill	100% Rectilinear

Table 5: Summary of significant printer settings

2.1.3. Printing

Prusa Mk3 printers were used for all printing. All samples were 3D printed using white E-PLA from Add:North, who produce their filament in Ölsremma, Sweden. Prior to print initialization, the printer was turned on and preheated to the standard PLA settings: 215°C nozzle temperature and 60°C bed temperature. When the target nozzle temperature was reached the filament was loaded into the printer. Before printing, the print bed was cleaned using ethanol (approx. 75% vol.). Ideally, window cleaner (Windex) should have been used, but this was not available in the print lab at the time of manufacturing. Printing was done directly on the smooth polyetherimide (PEI) standard Prusa print bed. After initiating the print, the process was monitored during first layer printing and was left to run with only intermittent inspection thereafter. After print completion and cool down of the samples, they were removed from the print bed and weighed.

2.1.4. Storage, conditioning, and preparation of samples

After printing, the samples were placed in zip-lock bags with a desiccant for at least 24 hours before testing. Digital image correlation was used during the testing of the optimized and reference samples produced in E-PLA. These samples were therefore speckled using generic black and gray acrylic spray paint 24 hours before testing and left to air dry before being returned to the bags.

2.2. Testing of the samples

2.2.1. Testing apparatus

All samples were subjected to the same flexural test on an Instron 5966 universal tester. A 5kN three-point bending fixture was used. Force measurements were made with an Instron 10kN load cell attached to the cross head. Experiment control and data acquisition was done with the integrated Instron/Blue Hill software. Data was logged at 2Hz.

Digital image correlation (DIC) was used during the testing of the topology optimized and reference sample. A Teledyne Genie Nano 5GigE M4040 Mono camera was used for image capture. A Fujinon CF50ZA-1S 1:2.4/50mm lens was mounted on the camera. The camera was mounted on a tripod with a micro-adjustment interface. During all tests, the camera was kept perpendicular to the specimen with approximately 25 cm from the front of the lens to the specimen. GenICam software was used for image acquisition. The framerate was 2 frames per second, except for one test run at 120 frames per second. Viz-2D DIC software was used for image analysis. Lighting was provided by three movable LED sources. No calibration image was used for the DIC. Correlation was conducted on all captured images for each specimen, except for the series taken at 120 frames/sec. In some of the series there was significant rigid body motion of the specimen, leading to unreliable measurements from the DIC. Attempts to use the software to remove rigid body motion failed for unknown reasons.

During processing of the captured images in the DIC software, a region of interest (ROI) was selected. This region of interest corresponded to the surface of the geometry. Any openings in the surface were removed from the ROI. Before running the DIC analysis, the ROI was checked for positional uncertainty using the software. The subset size was adjusted for some samples, to strike a balance between the lowest mean uncertainty and relatively even values across the surface. In most cases the subset size was set to 125. Incremental correlation was not used, and the software was set to analyze the entire ROI. The default processing parameters were used in the software. Pixel resolution was approximately 50 pixels/mm.

2.2.1.1. *Brief description of digital image correlation*

Digital image correlation (DIC) is an optical method for measuring deformations of objects or structures under the influence of loads. DIC can be 2D, using one camera, or 3D, using

two or possibly more cameras. A pattern is applied to the surface of the object being analyzed. This pattern is usually stochastic with a random distribution and size of pattern components, within an interval. During testing, the camera(s) capture images of the pattern on the object. These images are analyzed with software that uses machine vision algorithms to recognize points on the pattern surface and track their absolute and relative movement. This data can then be used to create different fields, for example strain or displacement fields, that can be mapped onto the surface image or used in calculations. (Sutton 2008).

2.2.2. Test setup

The bottom supports of the three-point bending fixture had a span separation of 70 mm during testing. Crosshead movement was set to 1mm/min. Samples were centered on and perpendicular to the bottom supports with the crosshead directly over the sample mid-point and perpendicular to it. Before testing commenced, the crosshead was brought into contact with the sample until the load cell registered contact. No other preloading was applied to the samples. The load cell and crosshead displacement were zeroed before beginning the test. Testing and DIC acquisition were initiated manually and, to the best of the operator's ability, simultaneously. Testing was carried out until failure of the sample or until the registered force dropped by 40%.

2.2.3. Measurements

The force-displacement data from the universal testing machine is used to calculate the stiffness of the samples through the relationship:

$$k = \frac{F}{\delta}$$

Where k is the stiffness, F is the force and δ is the displacement. This stiffness measure is equivalent to the slope of the force-displacement graph. Assessment of the optimized geometries performance will be based on this stiffness measure, instead of the Young's modulus. Relative strain data is available from the DIC. A comparison with strain data from simulations will be covered in the following analysis. Since the simulation corresponds fairly well with the experimental data, at least in the linear elastic region, some general remarks about the mechanical response of the optimized geometries can be made.

2.3. Simulation

2.3.1. Finite element simulation of geometries

The topology optimized and reference samples were simulated using finite element analysis in Abaqus. Attempts were made to simulate the lattice geometry, but due to time constraints a valid method for simulation was not found. Topology optimization results were exported from Abaqus as INP files, representing the optimized geometry with postprocessing (smoothing and filtering). Simulation models were created from these geometries.

2.3.2. Simulation setup and execution

Before importing the mesh representing the optimized geometry, the element type was manually edited in the INP file. Abaqus automatically saved the elements as S3, 2D shell elements, when the geometry was exported. Elements were manually changed to CPE3, plain strain solid 2D elements. The INP file was then imported as a model into Abaqus. Geometry representing the supports and crosshead of the three-point bending fixture on the Instron 5966 was copied from the original model used for optimization.

A solid isotropic material, based on the data available from Add:North's material datasheet for E-PLA, was applied to the section. Add:North specifies a flexural modulus of 3155 MPa and a tensile modulus of 2870 MPa (Add:North 2019). Initially the tensile modulus in the material model was set to 2800 MPa. This produced simulation results with higher stiffness than found in the experiments. Several values were tested, and a tensile modulus of 2400 MPa gave simulation results close to, but lower than, the experimentally measured values. A more precise value could be found in the interval between 2400-2500 MPa, but the value used in the simulations was kept at 2400 MPa.

While the elements were 2D solid, their section was given an out of plane thickness of 10 mm in the simulations, equal to the out of plane thickness of the 3D printed structures. Adding thickness to the simulated geometry allowed for the correct calculation of forces, so the simulations could be compared with the experimental results.

The interaction between the mesh and the analytical surfaces, representing the supports and crosshead of the testing apparatus, were defined using surface to surface contact. Surfaces were created on the mesh for this purpose. Friction was added to the interactions, with a coefficient of 0.2. On the left, bottom support a set of nodes on the mesh surface was

defined. Bonding between the mesh and analytical surface was limited to this set of nodes. The other contact surfaces had no such limitation applied. All the analytical surfaces were used as master surfaces, while the mesh surfaces were slave surfaces.

Boundary conditions were used to constrain the meshes downward movement. The two analytical surfaces representing the bottom supports were restricted from translation in both axes, and from rotation about the out of plane axis. Loading of the structure was done by displacing the top analytical surface, representing the crosshead. This displacement was done in two steps, an initial displacement of 0.05 mm in the negative y direction to close any gaps between the bodies, and a secondary step of 2.5 mm of displacement in the negative y direction. After trials with only one load application step, it became apparent that two steps were necessary to avoid analysis failure, or unexpected rigid body movements of the mesh. While the initial optimization process was based on a displacement of 1 mm, failure of the samples during testing happened after 2mm of displacement. To have a larger set of points to compare with testing, the simulations were conducted to 2.5 mm of displacement.

A non-linear geometry solver was used for the analysis. Displacement was introduced incrementally through time steps. For the first displacement step, the initial, minimum, and maximum increments were 0.1, 1E-5, and 0.5, respectively. In the second displacement step, these values were 0.01, 1E-5, and 0.05.

None of the mesh geometries were remeshed, except for one convergence test on the SIMP 0.30 volume fraction geometry. While all the meshes did have a few elements of poor quality ($\approx 1-1.5\%$), the convergence analysis showed that this had little effect on the result of the analysis.

After running the finite element analysis, force and displacement data was exported for comparison with the experimental data. Plots of strains and displacements were also exported, for certain displacement values of the crosshead, but will not be presented in this thesis. A qualitative comparison of the DIC strain results with simulation results will be made for one case in the 'Results' chapter.

2.4. Other tools

The software nTopology was used for assessing the volume of topology optimized geometry represented by the STL files used in 3D printing. nTopology was also used for conducting homogenization of the unit cell for the lattice geometry. This homogenization has only been used to generate the image for figure 6. This was for comparison with, and corroboration of, the measurements done in the PrusaSlicer software. nTopology is a software package for 3D design, modelling, and production of advanced 3D geometries, such as lattices and field-driven geometry.

3. Results

In this chapter results from the experiments and simulations will be presented. Mass analysis will be conducted on the 3D printed samples. The results of the three-point bending test will be presented and analyzed. Results from the three-point bending, digital image correlation (DIC), and simulation will be compared and analyzed. Some observations of lattice failure modes will also be presented and discussed.

3.1. Experimental results

3.1.1. Sample mass analysis

All samples were weighed before testing. The mass fraction ratio m_f is expressed as:

$$m_f = \frac{m_i}{m_r}$$

Where m_i is the average mass of optimized sample group i , and m_r is the average mass of the reference sample group.

From table 6 we can see that the mass fractions of the optimized geometries are all higher than the value given for the final volume fraction in the optimization parameters in Abaqus. The STL file for the SIMP 70% geometry has been studied using the PrusaSlicr and nTopology software. Volume was measured at 11877.85 mm³ and 11876.27 mm³, respectively, corresponding to a 0.742 volume fraction. This is close to the measured mass fraction for the SIMP 70% group, at 0.75, indicating that the excess mass, or volume, is likely due more to filtering and post-processing in Abaqus than from the manufacturing process.

Sample group	Average mass (g)	Mass fraction (-)	Volume fraction parameter (-)
SIMP70	14.79	0.75	0.70
SIMP60	12.84	0.65	0.60
SIMP50	11.01	0.56	0.50
SIMP40	8.79	0.45	0.40
SIMP30	6.86	0.35	0.30
RAMP70	14.54	0.74	0.70
RAMP60	12.61	0.64	0.60
RAMP50	10.70	0.54	0.50
RAMP40	8.73	0.44	0.40

RAMP30	6.65	0.34	0.30
Lattice 1	7.74	0.39	-
Lattice 2	7.97	0.40	-
Lattice 3	9.85	0.50	-
Reference	19.69	1.0	-

3.1.2. Results three-point bending: Stiffness

Figure 14 shows the force-displacement plots for all samples tested. There is a general trend in the data for the stiffness to be proportional to the volume fraction of material. In general, the initial data indicates that the SIMP specimens are stiffer for the 0.30, 0.50, 0.60, and 0.70 volume fractions, while the RAMP geometry is stiffer than SIMP for the 0.40 volume fraction. The peak bending load also seems to be higher for the 0.50, 0.40, and 0.30 volume fractions for the RAMP specimens.

Judging from the graphs of the initial testing data, the 0.70 SIMP and RAMP samples seem to be as stiff as the reference sample, at least in the linear elastic region. This observation is contradictive to a reasonable assumption that the unmodified reference should be the stiffest geometry. Statistical analysis will be used to test whether this observation is significant.

Linear regressions have been conducted on all the sample groups for the region that seems to be linearly elastic, between 0.3-1.3 mm of displacement. There may be some plasticity effects in this region, but they seem to be relatively small and are therefore disregarded. Ordinary least squares linear regression has been conducted using the stats.models.api OLS module in Python. All the data points from the tests conducted on each sample group have been used as the input, with displacement data as the independent variable and the force data as the dependent variable. The OLS module provides the best fit slope coefficient, as well as a 95% confidence interval for this coefficient. Since the slope of the graph is equivalent to the stiffness of the specimen, the slope coefficient from the linear regression can be used as a measure of specimen stiffness in the linear elastic region.

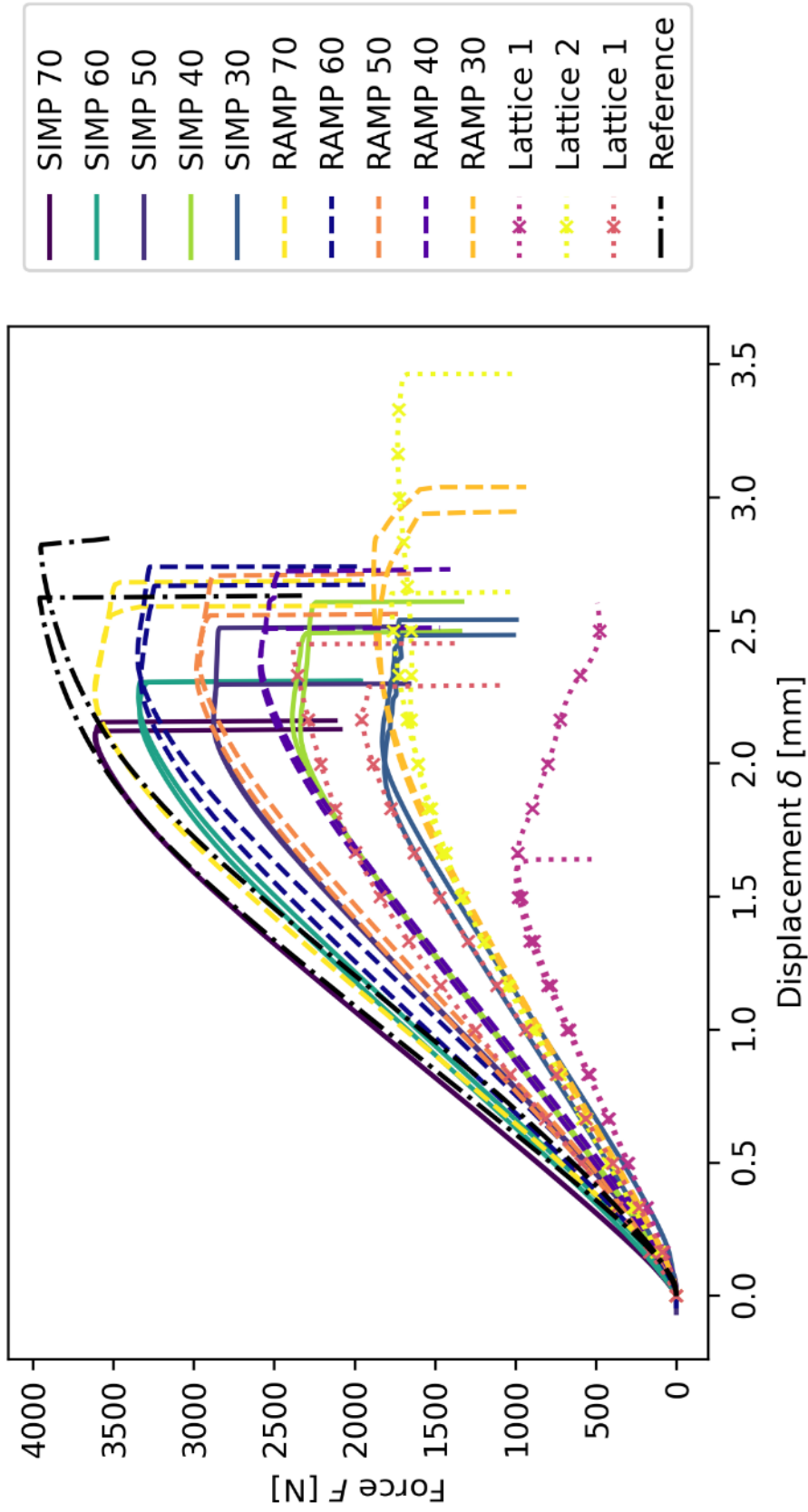


Figure 14: Results from three-point bending experiments on all geometries.

Table 7 lists the mean slope coefficient values, and the 95% upper and lower bounds, from the linear regression analysis. A relative stiffness measure k_r can be found by:

$$k_r = \frac{\bar{k}_i}{\bar{k}_{ref}}$$

Where \bar{k}_i is the mean slope coefficient for sample group i , and \bar{k}_{ref} is the mean slope coefficient for the reference sample group. Calculating k_r shows that its value is higher than the sample groups' respective volume fraction.

Reviewing the raw experimental data gave the impression that the SIMP 0.70 volume fraction samples were equally as stiff as the reference. The results from the regression analysis show that the SIMP 0.70 slope coefficient 95% confidence interval is entirely within the 95% confidence interval for the reference samples. Additionally, the SIMP 0.70 mean is located close to the mean of the reference sample interval. Given the null hypothesis that $\beta_0 = \beta_1$, i.e. that the slope of the reference linear regression graph is equal to the slope of the SIMP 0.70 graph, we are compelled to accept this hypothesis. In other words, given the collected data, the SIMP 0.70 samples are equally as stiff as the reference samples. This is likely due to there being a relatively small decrease in material compared to the reference, and that the removed material was carrying only a small fraction of the load. Reducing the volume fraction below 70% does result in a decrease in stiffness. Yet, since the algorithm only removes the material that is contributing the least to the stiffness of the structure the relative stiffness k_r is greater than the corresponding volume fraction v_f for any given sample group in this experiment.

The stiffness of the RAMP 70% volume fraction samples was also very close to the reference, yet their 95% confidence interval lies completely outside the 95% confidence interval for the reference sample. It seems safe to conclude that the RAMP 70% samples are less stiff than either the SIMP 70% or reference samples.

Sample group	Lower 95% bound	Mean	Upper 95% bound	k_r
SIMP70	1989.9	1991.64	1993.39	~1
SIMP60	1778.46	1791.28	1804.09	0.906

SIMP50	1578.217	1581.6563	1585.095	0.800
SIMP40	1268.619	1271.5744	1274.53	0.643
SIMP30	1017.848	1038.5387	1059.229	0.526
RAMP70	1922.648	1925.2811	1927.914	0.974
RAMP60	1680.668	1706.6444	1732.621	0.864
RAMP50	1499.229	1512.2596	1525.29	0.765
RAMP40	1283.172	1292.1283	1301.085	0.634
RAMP30	941.127	944.8297	948.533	0.478
LE1	724.112	727.054	729.996	0.368
LE2	944.252	948.8398	953.427	0.480
LE3	1127.858	1188.885	1249.912	0.602
Reference	1933.334	1976.2119	2019.09	-

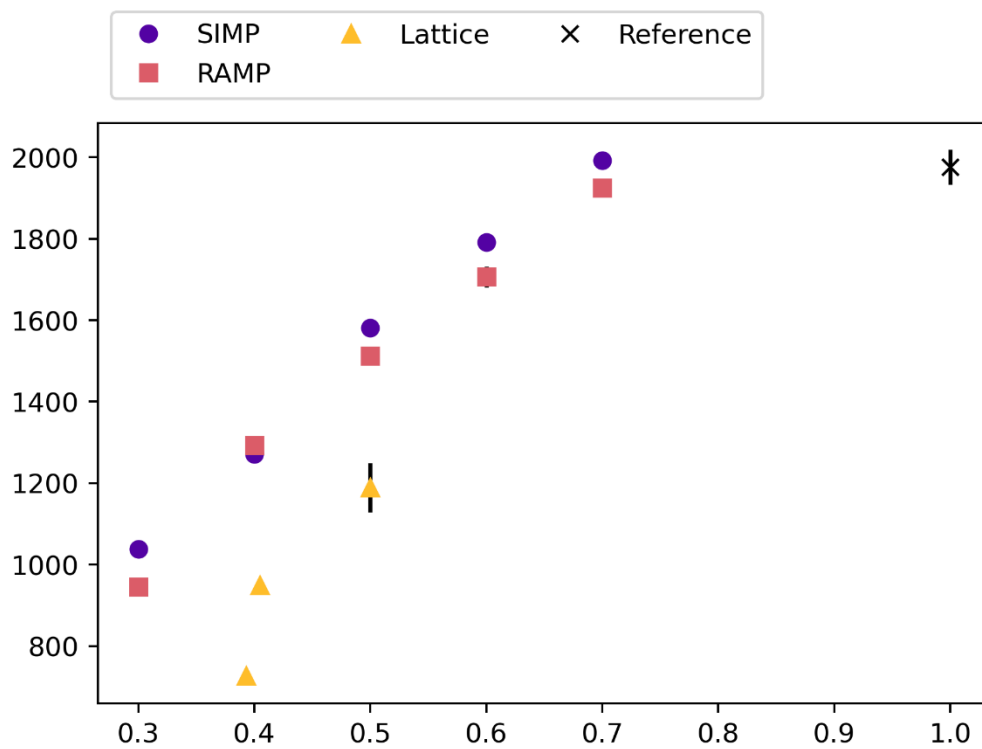


Figure 15: Plot of sample stiffness with error bars. Most of the sample groups displayed low variance in measured stiffness, except for Lattice 3 and the reference.

Other observations from the statistical analysis confirm the initial impression that the SIMP geometries are stiffer than RAMP for all volume fractions except 0.40. This conclusion is based on the observation that the 95% confidence intervals for the SIMP 0.30, 0.50, 0.60,

and 0.70 volume fractions are completely outside, and have higher values than, the intervals for the RAMP samples at corresponding volume fractions.

3.1.3. Results three-point bending: Stiffness

The efficiency of optimization methods can be based on a comparison of the specific stiffness of the specimens, i.e. the stiffness over the density. In figure 16 the absolute stiffness k of the samples has been plotted, together with the specific stiffness. Absolute stiffness is the ratio:

$$k = \frac{F}{\delta}$$

Where F is the force, and δ is the displacement, with units $[N/mm]$. Specific stiffness k_s is commonly the ratio:

$$k_s = \frac{k}{\rho}$$

Where ρ is the material density. For this analysis, a modified measure of specific stiffness is used:

$$k_s = \frac{k}{\rho \cdot m_f} \text{ or } k_s = \frac{k \cdot V}{m}$$

Where m_f is the mass fraction of a sample group compared to the reference sample, V is the volume of the reference geometry, and m is the average mass of a sample group. The units can be

$N \cdot mm^2 \cdot kg^{-1}$ or more generally $l^3 \cdot t^{-2}$ (length cubed, one over time squared).

The measured material density of the E-PLA used to print the samples was calculated to 1.231 g/cm^3 , based on the reference sample with a volume of 16 cm^3 and average mass of 19.69 grams.

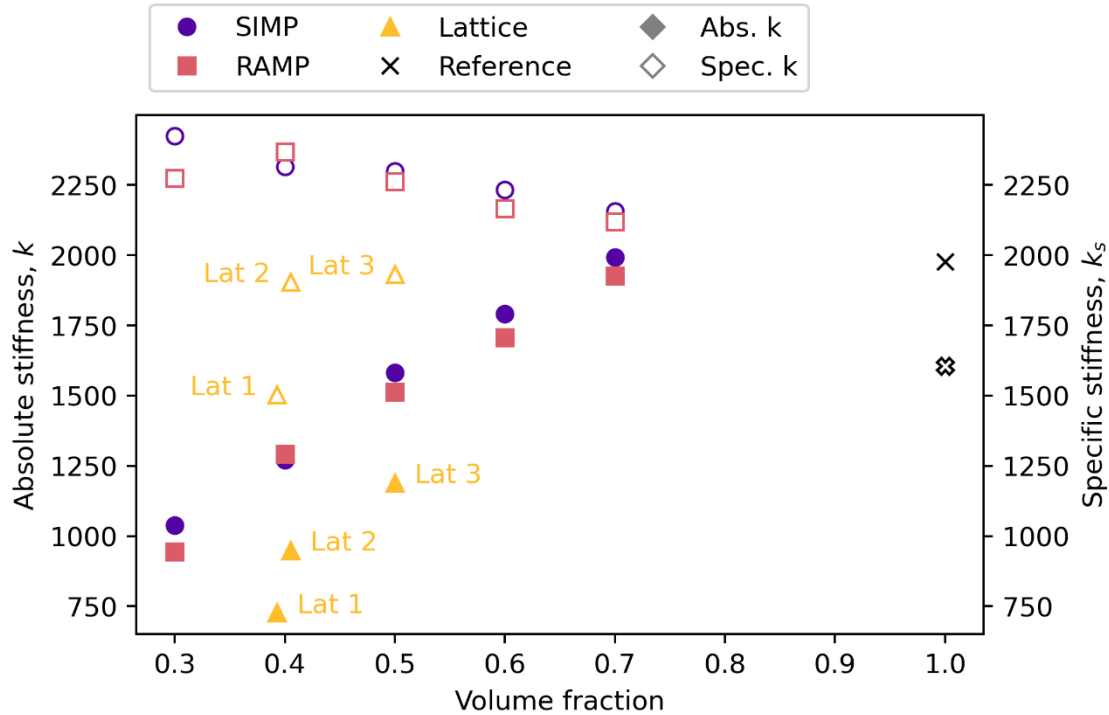


Figure 16: Plot of absolute and specific stiffness

From the graph we can see that the absolute stiffness is proportional to the volume fraction of material in the optimized structure. When looking at the specific stiffness, it is apparent that the optimized structures outperform the reference geometry. This tendency increases with decreasing volume fractions. There seems to be a peak in the specific stiffness of the RAMP samples at the 40% volume fraction, while the SIMP samples display a continuous increase in specific stiffness with decreasing volume fraction. All the lattice geometries were significantly less stiff than the topology optimized geometries when compared on a mass fraction basis. Yet, they have higher specific stiffness than the reference.

3.1.4. Results three-point bending: Load capacity

The load capacity is the maximum measured force value that the specimens withstood in the three-point bending test. This value was found in the region of combined elastic and plastic deformation and is found in the flat region of the force-displacement curve and near the onset of failure.

The absolute load capacity reported here is the average maximum force from the two samples in each sample group. The specific load capacity l_{c_s} has been calculated by:

$$lc_s = \frac{F_{max}}{\rho \cdot m_f}$$

Where F_{max} is the maximum force registered.

The absolute load capacity of the geometries decreases with decreasing volume fractions. Data for the specific load capacity indicates that all topology optimized geometries outperform the reference on this measure. RAMP geometries have consistently higher specific load capacities than SIMP. There seems to be a peak in the specific load capacity at the 40% volume fraction for both SIMP and RAMP specimens. The lattice geometries have consistently lower absolute and specific load capacities than either of the topology optimized groups, but lattices 2 and 3 outperform the reference when comparing specific load capacity.

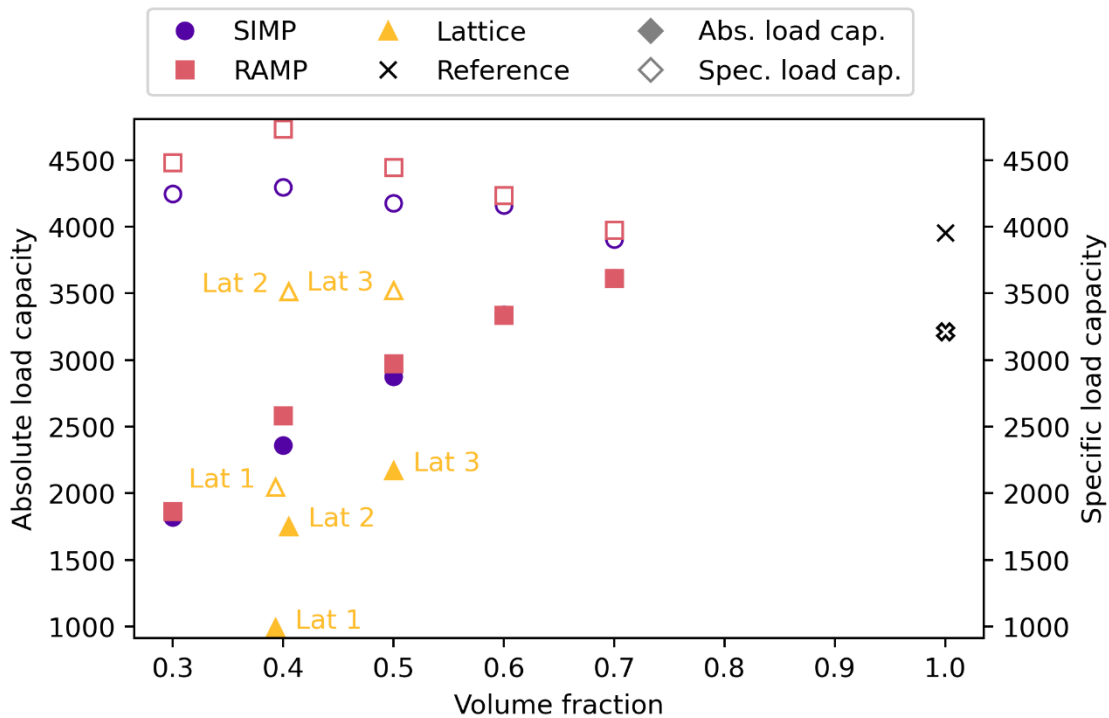


Figure 17: Absolute and specific load capacity lc

3.1.5. Results three-point bending: Work of fracture

Here work of fracture (U) is defined as the area under the force-displacement curve, or the amount of work the structure can withstand before final failure. Resistance has been calculated using the trapezoid method for numerical integration. Each data point from the three-point bending test consists of a displacement (x) value and a force (y) value. The

spacing of the x values are slightly irregular, so the integral has been computed without a single value for Δx . The following formula was used:

$$U = \int_A F d\delta \approx \frac{1}{2} \sum_{i=1}^n (y_n + y_{n-1})(x_n - x_{n-1})$$

The specific resistance U_s was calculated by:

$$U_s = \frac{U}{\rho \cdot m_f}$$

Comparing the absolute work necessary for failure of the structures, the reference sample outperformed all optimized geometries. Looking at the specific work, another pattern emerges. RAMP samples significantly outperformed the SIMP samples when comparing volume fractions. Additionally, all volume fractions of the RAMP samples outperformed the reference sample when comparing specific work. The SIMP 70% volume fraction had lower specific resistance than the reference, the 60% fraction was on par with the reference, while the remaining had higher specific resistance. There seems to be a peak in the specific resistance of the SIMP samples at the 40% volume fraction. For the RAMP samples, the resistance increased with decreasing volume fractions, albeit the incrementation varies. See figure 19.

An interesting observation is the specific resistance of the Lattice 2 geometry. It had the second highest specific resistance of all the samples. This group did display high variance in the measured resistance, but it seems likely that this lattice structure can absorb substantial mechanical work before failure. Reasons for this will be addressed more closely in the section on lattice failure modes, but in short it seems that local failure of the lattice is less detrimental to the global structural performance than for the topology optimized samples. Figure 18 shows an example of local buckling failure that does not lead to global failure in Lattice 2. Energy is absorbed through this buckling mechanism. The stiffness of the structure is lowered, but it can still withstand load.

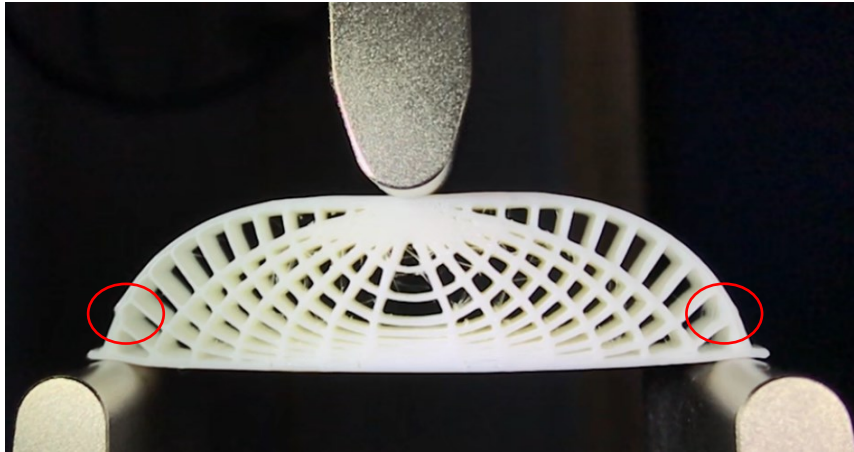


Figure 18: Lattice 2 local buckling failure, without global failure.

The other lattice geometries had lower absolute and specific resistance than the topology optimized geometry when comparing volume fractions. They also had lower performance than the reference, both in absolute and specific terms.



Figure 19: Absolute and specific work of fracture U .

3.2. Results from finite element simulation

In this section, the results of finite element simulation will be presented. There are three main objectives in this section. One is to compare the simulation results with the Instron data to judge if there is reasonable agreement between them. Second, the simulations will

be compared with the digital image correlation (DIC) results for strain. Finally, if there is reasonable agreement between the simulations and these two experimental data sets, then comparison of the strain results from the simulations can be made.

3.2.1. Simulation results: Force-displacement graphs

From figures 20 and 21 we can see that there is a reasonable agreement between the experiments and the simulations when comparing force and displacement data, at least in the linear elastic region. All the simulations underestimate the stiffness of the geometries, but more so for SIMP than RAMP. This is mainly due to the material properties used in the simulation, where the Young's modulus is lower than it ideally should be. As mentioned previously, a more precise value for the Young's modulus could be found, but it would unlikely effect the results significantly.

Final failure of the samples has not been modelled, as this would require a plastic material and failure model. The finite element model seems to be accurate for the linear elastic region.

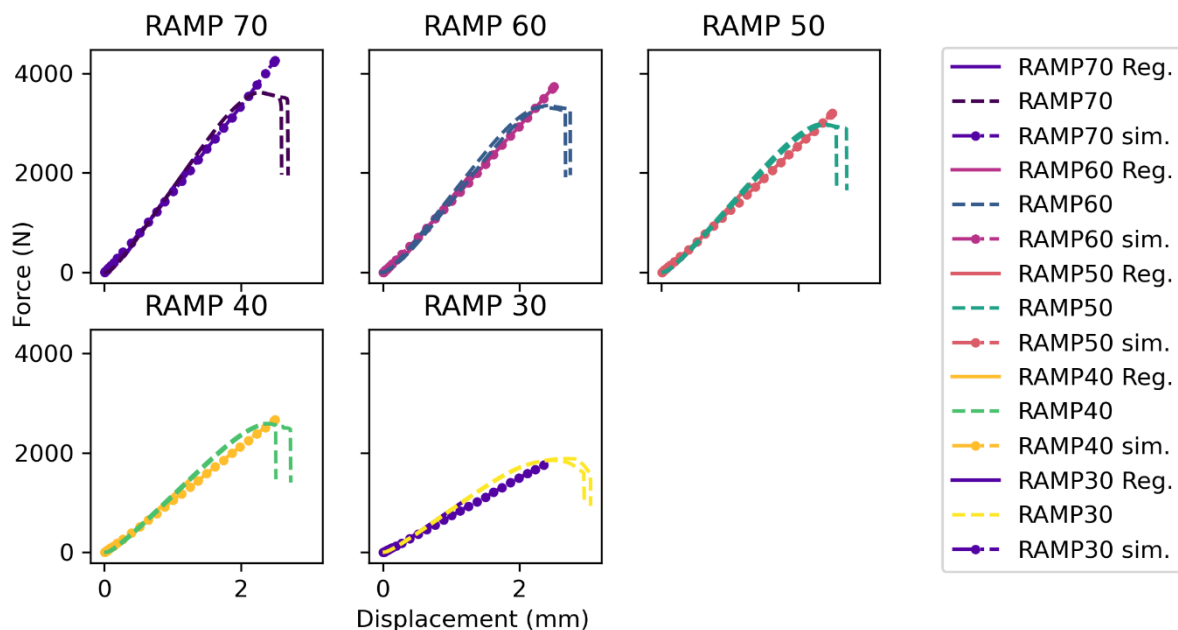


Figure 20: Simulation results for RAMP samples, plotted with experimental data and regression results.

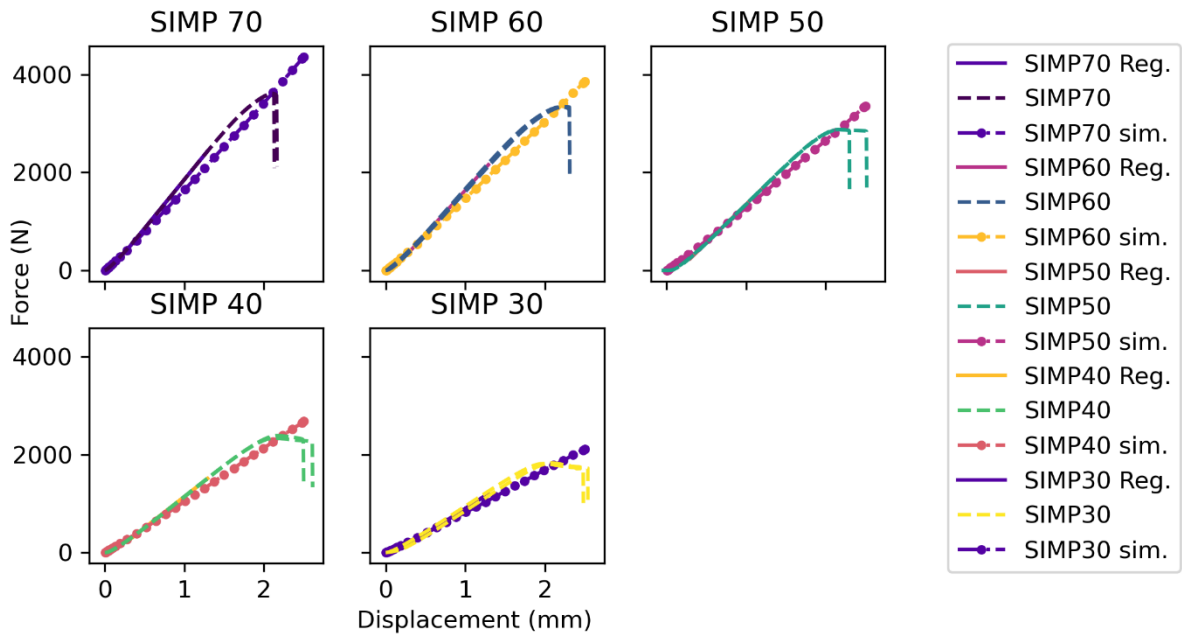


Figure 21: Simulation results for SIMP samples, plotted with experimental data and regression results.

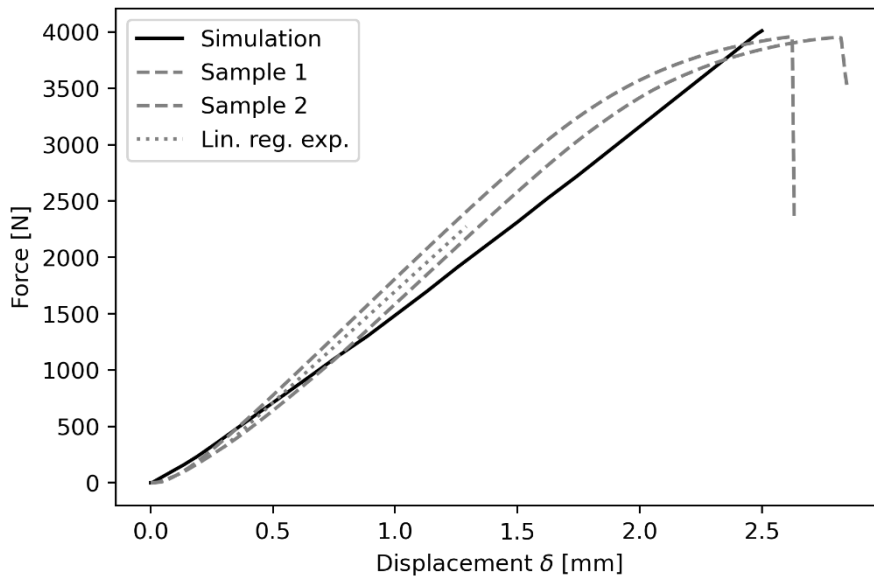


Figure 22: Simulation results for reference samples, plotted with experimental data and regression results.

3.2.2. Simulation results: Stiffness of SIMP 70, RAMP 70, and reference
 In the experiments, the SIMP 70%, RAMP 70%, and reference samples all had very close stiffness values. Comparing the simulation results we can see the same tendency. The element shape could explain the observed simulation results to some extent, as the

meshing of the SIMP and RAMP models was more triangular, while the reference model had only quadrangular elements.

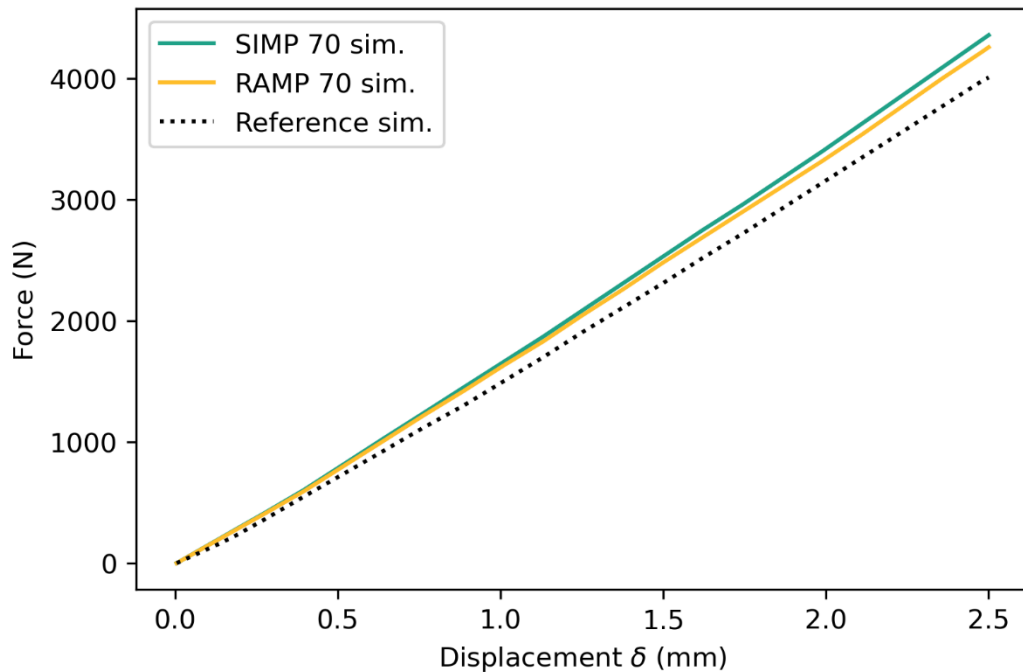


Figure 23: Comparison of simulation results for SIMP and RAMP 70% volume fractions, and the reference geometry

3.2.3. Convergence analysis simulation results

A convergence analysis was conducted on the simulation of the SIMP 30% volume fraction sample to uncover if the mesh used in the simulations of all the geometries could have influenced the result. The SIMP 30% geometry was chosen as it has the thinnest sections, where mesh effects would have the greatest impact. Three different meshes were tested on the geometry, the original mesh, a modified mesh with 0.50 mm edge length, and a final mesh of 0.25 mm edge length. The elements of the remeshed geometry were predominantly triangular, with some hybridization with quadrangular mesh. All other simulation parameters were the same for the three meshes. Remeshing the geometry had no significant effect on the results of the simulation. Figure 24 shows the force-displacement graph for all three meshes and the SIMP 30% volume fraction regression line. As we can see, the largest error in the simulation is from the stiffness of the material model, not the mesh. The greatest difference between the simulation results of the meshes is in the

region of plastic deformation in the experiments, and the entire model is inaccurate in this region anyway.

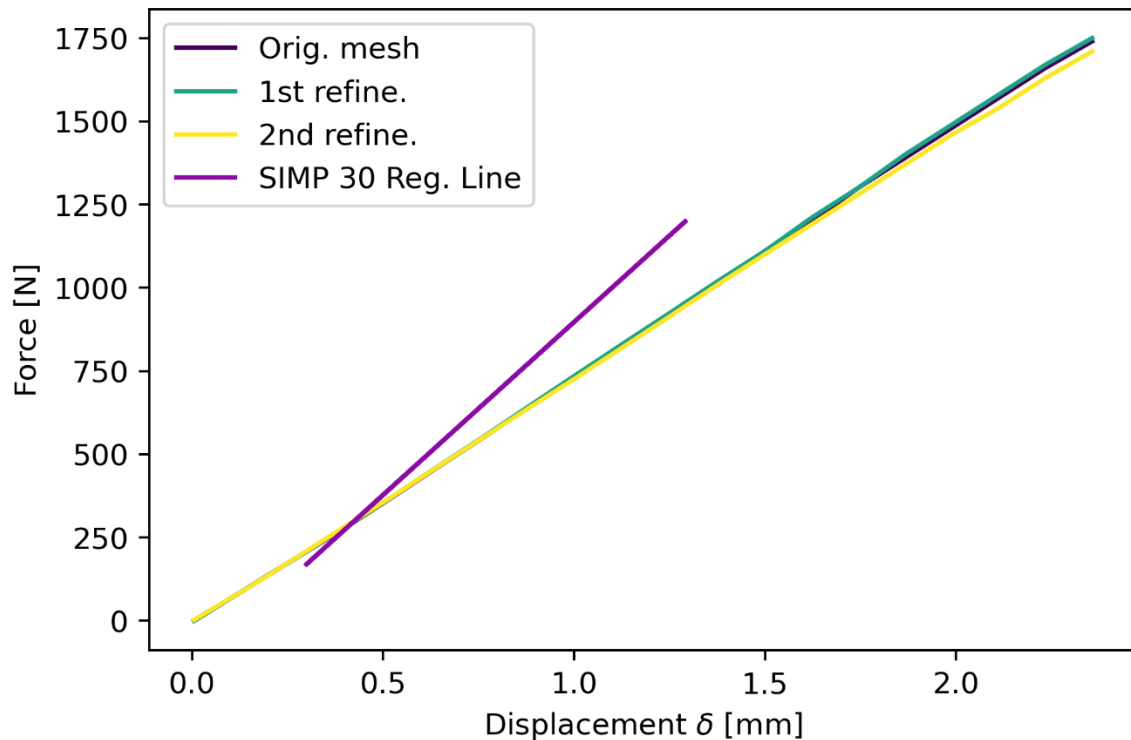


Figure 24: Results of convergence analysis on the SIMP 30% volume fraction geometry.

3.3. Simulation results and DIC

Both the simulations and the DIC provide a large amount of data and images. It is beyond the scope of this thesis to present and review this material in its entirety. For the sake of brevity, only one case will be included. Given the quality of the DIC results from the SIMP 60% volume fraction tests, this has been chosen as the case. In the experiments, the samples failed due to cracks forming on the bottom of the specimen, near the midpoint, and propagating towards the crosshead of the fixture. Principal tensile strain can reveal the failure mechanisms at work in the sample. The DIC and simulation results for the principal strain ϵ_{\max} (in simulation) or ϵ_1 (in DIC) have been chosen for this case, as they illustrate the tensile strains clearly. DIC strain field images provide an indication of plastic deformation, and crack formation and propagation prior to cracks becoming visible macroscopically.

Figures 25 and 26 are graphical representations of the strain fields from DIC and simulation. The images on the left are from DIC, on the right from simulation. From the top, the images correspond to 0.5, 1.0, 1.5, 2.0, and 2.31 (failure) mm of displacement. The graph at the bottom shows where the images are taken from on the stress strain curve for both the

experiment and the simulation. In the images we can see a reasonable agreement between the DIC and simulation images in the linear elastic region. While the color coding is not consistent between the DIC and the simulation, the strain values are relatively close, and the contours are rather alike in the linear elastic region.

There are small asymmetries in both the DIC images and the simulation results. The DIC images have larger asymmetries than the simulation results. This is mostly due to minute errors in placement of the sample on the fixture, unequal lighting, and image noise. Some of the asymmetry also stems from the samples themselves not being perfectly symmetric. This is the main reason for the asymmetries in the simulation results. The asymmetries in the geometry are very small. Using nTopology, the left and right sides of the SIMP 50% volume fraction geometry was split in the middle and mirrored. Using a Boolean subtract, where the right-side geometry was subtracted from the left-side geometry, a volumetric difference of 0.53% was found between the two sides.

The last two DIC images are from the plastic region of the force-displacement graph. On the bottom of the specimen, we can see concentrations in the strain fields that are not present in the simulation. These concentrations in the strain field are indicative of increased localized strain, due to crack formation and propagation, and plastic deformation.

In the final DIC image we can see a clear indication of a crack extending from the bottom surface to the hole directly above it. Closer inspection of the last image captured before sample failure reveals one limitation of DIC. Comparing the highlighted region from DIC, which can be indicative of a crack, with the failed sample in figure 27 shows that the crack is probably just superficial, as it located to the left of the fracture line. The close-up image in the same figure shows the crack highlighted by DIC surrounded by a blue-green line. To the right of this crack is another crack, designated by the red arrow and encircled by the red dashed line, that is barely visible. This crack corresponds well with the observed fracture in the specimen. Large surface strains can mask significant features in DIC.

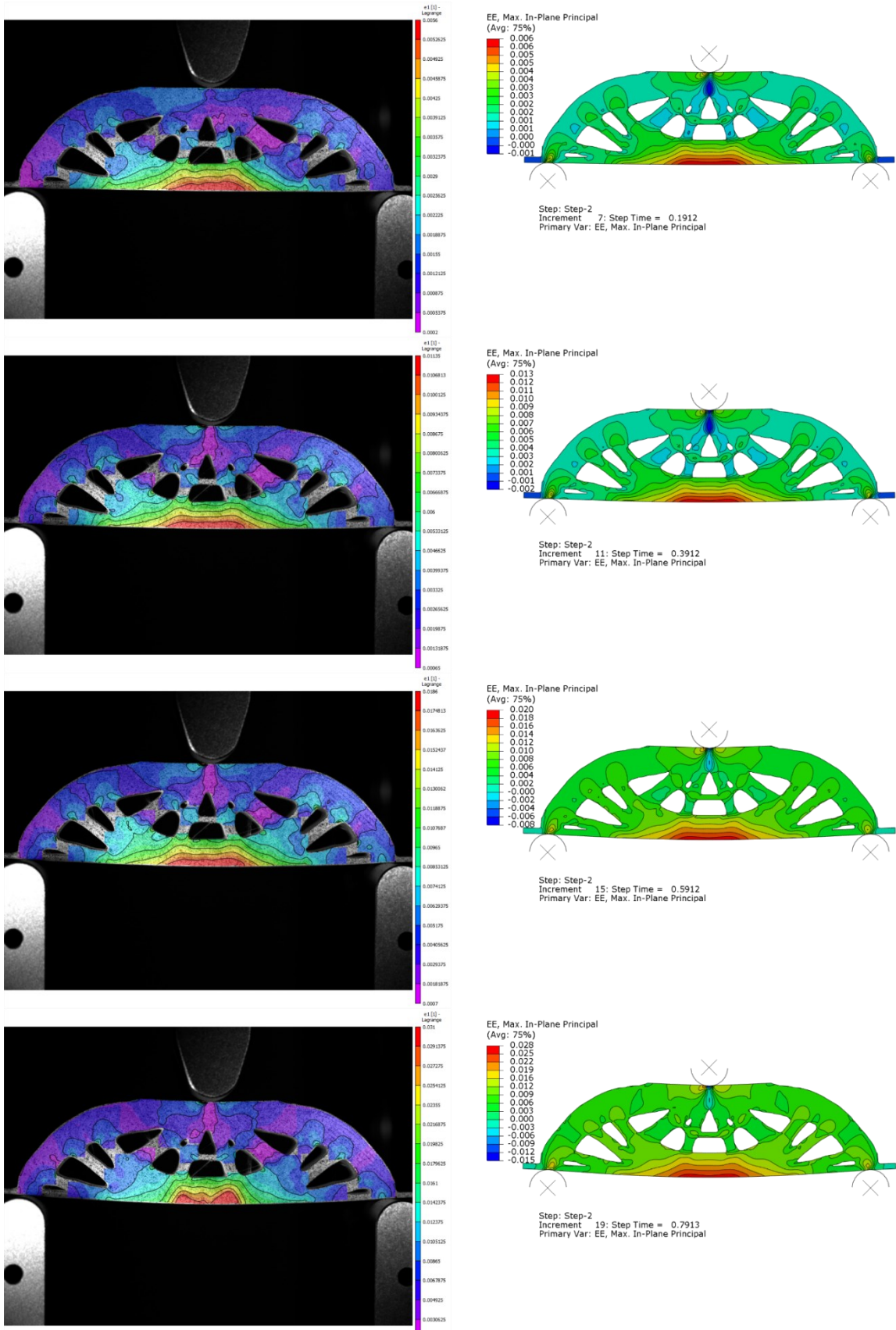


Figure 25: DIC (left) and simulation results (right) for principal strain ϵ_{max} for the SIMP 60% volume fraction. From top: 0.5, 1.0, 1.5, and 2.0 mm of displacement.

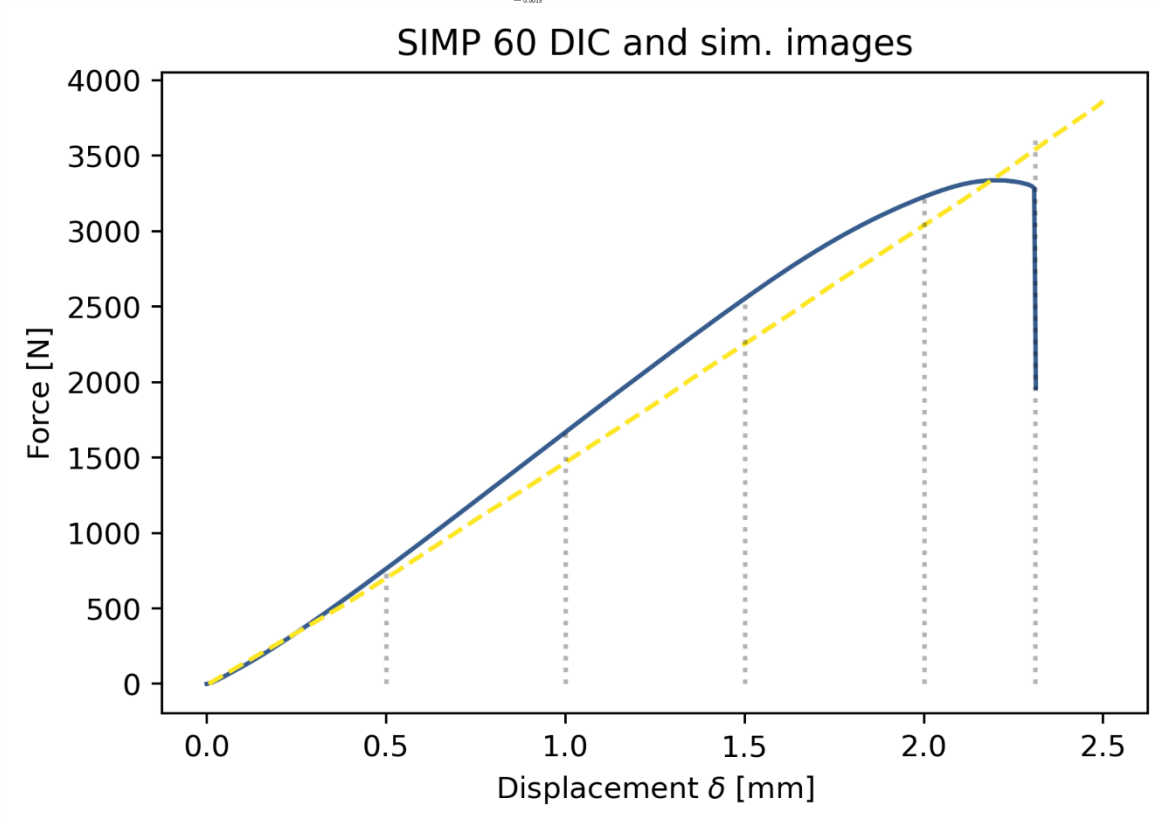
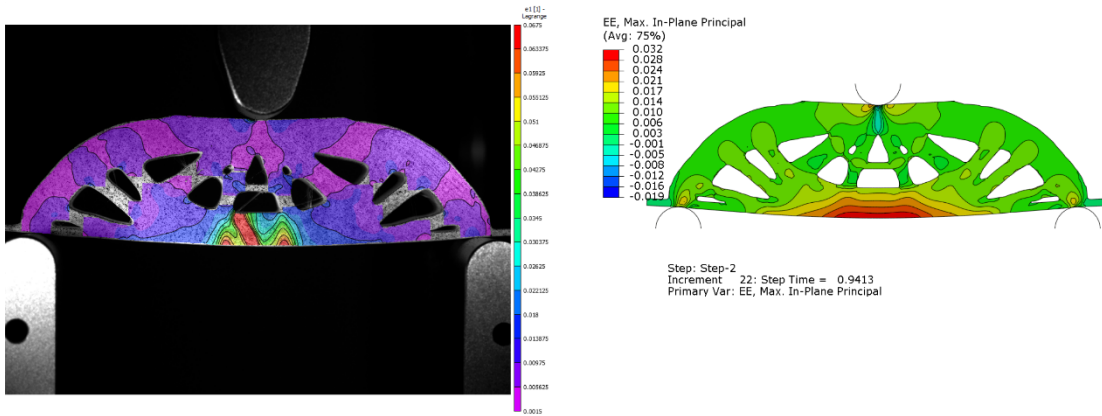


Figure 26: DIC (left) and simulation results (right) for principal strain ϵ_{max} for the SIMP 60% volume fraction at failure. Graph illustrates where the images have been captured on the force-displacement curve from the experiments (blue, solid line) and the simulations (yellow, dashed line).

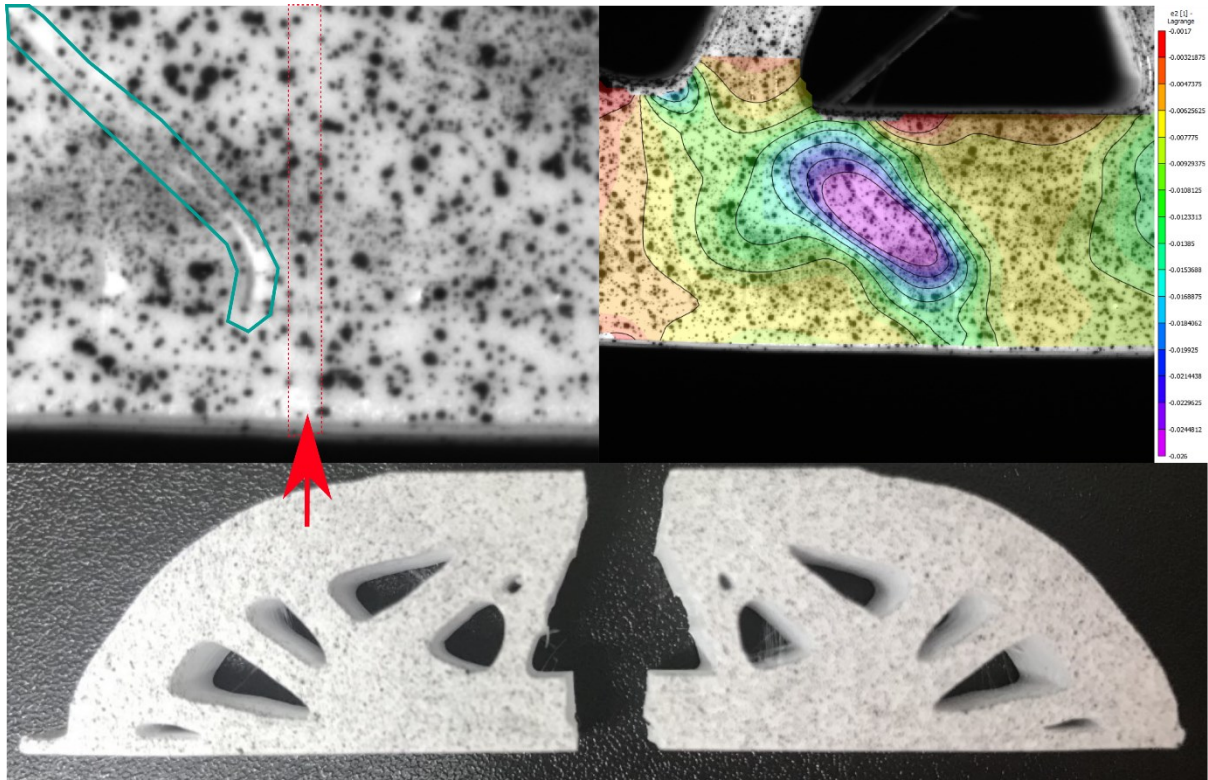


Figure 27: Comparison of DIC result with sample failure. DIC (top, right) indicates a crack (area of high concentration of contour curves), which is only superficial. The fracture happens along a crack not indicated by the DIC. The top, left image shows the surface crack marked by the blue-green line. The red arrow and dashed line indicate a faint crack that corresponds to the final fracture surface. Bottom: Fractured sample.

3.4. Failure of topology optimized and lattice structures

Comparing the force-displacement graphs for lattice geometries 1 and 2 with those for the topology optimized geometry shows that the plateau region, after the linear elastic region and before failure, is substantially larger for these lattices. This is not the case for lattice 3. Failure in the topology optimized geometries was seemingly abrupt and happened globally, i.e. the entire structure failed. The DIC does reveal that plastic deformation, and crack initiation and propagation take place in the plateau region of the topology optimized geometries. Failure in these structures occurs when the crack growth becomes unstable, that is when the change in the energy release rate becomes greater than the change in resistance of the material ($\frac{dG}{da} > \frac{dR}{da}$), assuming that the fracture resistance increases with crack length, which seems likely.

In lattices 1 and 2, failure was more complex. As mentioned briefly in the section on work of fracture, the failure of these two lattices was initially dominated by localized buckling of the lattice members. During this phase of localized failure, the structure maintains a certain fraction of its original carrying capacity and stiffness. After the phase of localized buckling,

lattice 1 and 2 behaved differently. In one of the experiments, lattice 1 never reach global failure. The experiment stopped because the one condition for ending the test was reached, namely that the load dropped by 40%. In the other experiment with lattice 1, final failure was by a through crack near the bottom support. Lattice 2 samples, on the other hand, failed globally, initially by crack propagation from the bottom surface. The crack initiation point seems to be located near where one of the compressive members meets the bottom tensile member. This could be an indication of shear induced failure, as intersection between compressive and tensile members would experience bending, especially when the structure has become deformed from its initial state.

Lattice 3 samples failed in two different ways. One of the samples had a print defect on the one side near the bottom support. The lattice had detached from the print bed during printing, leading to this area have lower thickness and out-of-plane curvature. This sample failed in this area by a crack initiating on the bottom surface. The other sample failed by a crack originating between the extruded polymer bead and parallel to it. This same failure mode was seen in lattice 3 geometry printed in another PLA material but was not included in this thesis. It seems likely that this failure mode is the dominant one for the lattice 3 geometry when manufactured using FDM/FFF 3D printing technology with PLA.

4. Discussion

4.1. Potential applications and further avenues of study for lattice structures

The failure behavior seen in lattices 1 and 2 points to some potential applications of lattice optimized structures. Using lattices for impact absorption has been documented (e.g. Ozdemir et al. 2016), as have stiffness optimized lattices (eg. Wu et al. 2021). Lattice structures could be optimized for a combination of stiffness and damage tolerance or impact absorption. For example, lattice structures that maintain a certain level of structural performance even after impacts or extreme loading conditions could be produced. It is beyond the scope of this thesis to study potential applications of lattices that combine these qualities any further, yet a few remarks on further investigations and implementations will be made. Optimization of lattice structures, using a homogenization approach like Wu et al. (ibid.), and combining stretch and bending dominated architectures (Deshpande et al. 2001), could realize lattice structures that can combine excellent structural performance with impact resistance and/or damage tolerance. In stretch dominated lattices, the unit cells experience axial forces predominantly, such as is the case in this thesis, while in bending dominated architectures the unit cells experience mostly bending forces (ibid.). Stretch dominated lattices are more mass-efficient in structural applications, i.e. they achieve higher stiffness per mass unit, while bending dominated lattices are better at absorbing energy (Alkhader et al. 2019). Both cell type and orientation influence the stretch-bending behavior of lattice structures. Optimization for combined stiffness and damage tolerance could utilize an approach with only one unit cell type, where manipulation of cell orientation alters lattice characteristics, or could combine two or more cell types to achieve the same goal.

4.2. Challenges

While topology and lattice optimization show promise for creating lightweight and strong structures, there are certain challenges that must be addressed before implementing such structures in practical applications, especially ones that are critical. Four such challenges will be discussed shortly here.

4.2.1. Fatigue life of topology and lattice optimized structures

Firstly, studying and quantifying the fatigue life of topology and lattice optimized structures is more complex than with traditional geometries and materials, especially for lattices.

Given that 50% - 90% of all mechanical failures are due to fatigue (Oest 2017, p. 5), the response to cyclic loading should be a significant factor when optimizing structures. Holmberg et al. (2014, p.207) point out that topology optimization, where stiffness is maximized for a given volume constraint, can lead to large stress concentrations that must be mitigated to achieve satisfactory fatigue life. Additionally, the fatigue analysis and structural modification must be carried out after the initial optimization process. Zhu et al. (2021) also point to challenges with fatigue life of optimized parts that are additively manufactured. Material anisotropy, surface quality, and geometry all contribute to compounding the problem of fatigue analysis of topology and lattice optimized parts.

Using fatigue as a criterion for optimization itself is challenging. Several sources report methods for including fatigue life as a design response in topology optimization. Lee et al. (2015) develop a topology optimization method that can minimize the volume fraction under a fatigue life constraint using a frequency domain approach. Liu et al. (2020) present a method for optimizing a regular cellular lattice for fatigue life. Oest & Lund (2017) present an optimization method that allows the use a fatigue life measure for cyclic problems that can be quantified with the rainfall method. Optimization with fatigue life constraints is an active area of research, with many more contributions than can be presented here. Many finite element software include stress-based optimization (e.g. Abaqus, SolidWorks, Fusion 360), but no sources could be found that indicate the existence of a fatigue life criterion for optimization in any commercially available package.

4.2.2. Qualification and quality assurance

A second challenge facing topology and lattice optimization for practical applications is qualification or quality assessment of manufactured geometry. Due to their geometric complexity, assessing additively manufactured, optimized parts can be difficult. Measuring and defining the acceptable deviations from the initial design may not be able to rely on standardized approaches in industry. Zhu et al. (2021, p.105) point to the need for additional research to enable the systematic and accurate characterization of optimized structures in general, and lattices in particular.

Looking at the samples studied in this thesis shows some of the issues relating to quality control. Creating a useful 2D technical drawing with dimensions of the geometries would be very difficult, if not impossible. Verification of the fabricated geometries could therefore not

rely on comparisons of parts with technical drawings. One possibility is to use digital imaging and 3D scanning technology (e.g. CT or laser) with machine vision algorithms to assess the external, and possibly also internal, geometry of fabricated parts. Such methods may also be able to uncover potential manufacturing defects. (Kim et al. 2018).

While checking for conformity between 3D manufactured parts and models is possible, this is not enough to ensure that additively manufactured topology and lattice optimized parts will perform according to models or experimental results. Defects and artefacts from the manufacturing processes affect the performance of parts. Predicting the behavior of additively manufactured structures, and especially small-scale objects such as lattices, is complex. Uncovering the relationships between observed defects, mechanical properties, and processing parameters may be even more so. Kim et al. (ibid.) point to the need for more research and development in these areas. Zhu et al. (2021) report the need for more research concerning process induced defects, such as residual stresses and thermally induced deformations.

4.2.3. Simulation of lattice structures

A third problem area that concerns lattice structures particularly is with conducting precise simulations. Since lattices can consist of many thin features, accurate simulation is computationally intensive if using finite element method. One common approach is to use homogenization, where the unit cell's elastic properties are measured for a limited set of loading conditions and intermediate values are interpolated from these measurements. These elastic properties are then applied to the entire lattice structure in simulation. Homogenization has limitations when applied to finite lattice structures, as well as when local deformations become large. (Zhu et al. 2021).

Tancogne-Dejean et al. (2019) report successful modelling, when compared to experimental results, of lattice structures undergoing large deformations and high strain rates. The geometry tested consisted of one unit cell with relatively large dimensions (10s of mm). They conclude that more experimentation is required to scale their results to larger structures. Scaling to smaller structures must also address effects arising from the manufacturing process, including surface roughness and manufacturing defects.

4.2.4. Topology optimization with manufacturing constraints

The final challenge facing topology and lattice optimized structures that will be discussed relates to manufacturing constraints. Zhu et al. (2021) point to unsupported overhangs, support structures, and enclosed voids among other things, that can affect the fabrication of lattice and topology optimized structures. In their paper, Zhu et al. (2021) present several sources that have developed methods for including manufacturing constraints in the topology optimization process itself, such as constraints on overhang angles or build orientation. Ideally 3D printed optimized structures should be self-supporting to avoid support structures that require excess material in manufacturing and labor during removal. Achieving this is an active area of research. Bartsch et al. (2019) introduce a method for combining topology optimization with process simulation to find optimal support structures that reduce material use in manufacturing as well as lowering the risk of thermally induced failure of prints. Some commercially available software can add manufacturing constraints in the optimization process. These constraints can be applied to overhangs, print direction, and minimum part thickness.

5. Conclusions

The results from the experiments and simulations indicate that the optimization methods reviewed in this thesis produce geometries that can achieve significant improvements in the mass-specific mechanical responses of structural elements. While these methods can produce complex geometries that may be difficult to manufacture using traditional methods, additive manufacturing technology can allow fabricating such structures. Two-dimensional optimized geometry, as has been studied in this thesis, could be produced with many conventional manufacturing technologies.

Depending on the requirements of a given structure, the choice of optimization method can have a significant impact on performance. In these experiments, only three performance indicators have been studied, stiffness, load capacity, and work of fracture. For the specific problem studied here, the selection of an optimization method would vary depending on the significance of each performance parameter. If selecting for stiffness, it seems the SIMP method would be the best choice. On the other hand, if work of fracture were more important, either the RAMP or lattice methods would be better choices. In Abaqus it is possible to add multiple objective functions, even weighted, for topology optimization. This has not been explored in this thesis, but it seems reasonable to assume that combining multiple optimization criteria may achieve results that address the specific structural requirements for an application. There are many possible optimization criteria that could be used – e.g. eigenfrequencies or thermal properties – in addition to stiffness or compliance.

This thesis makes no claims about the validity of the results for other optimization problems, geometries, or loading conditions. The findings suggest that, while topology and lattice optimization can give lighter parts with satisfactory performance, it would be prudent to test multiple optimization methods in simulation and experimentally to aid in the selection of an optimization scheme for a specific problem. Creating more complex simulation models, including plasticity and failure criteria, could aid in identifying the most promising optimization results for testing, thereby reducing the need for extensive experimentation.

6. References

- About structural optimization* (n.d.) viewed 12.05.2021. <https://abaqus-docs.mit.edu/2017/English/SIMACAEANLRefMap/simaanl-c-optover.htm>
- Add:North (2019) *E-PLA: Technical Data Sheet: Revision 2.1*. viewed 06.04.2021. https://storage.googleapis.com/addnorth-com-public/files/EPLA_TDS.pdf
- Alkhader, M; Nazzal, M; Louca, K. (2018) Design of bending dominated lattice architectures with improved stiffness using hierarchy in *Journal of Mechanical Engineering*. 233(11). <https://doi.org/10.1177%2F0954406218810298>
- Bartsch, K; Lange, F; Gralow, M; Emmelmann, C. (2019) Novel approach to optimized support structures in laser beam melting by combining process simulation with topology optimization in *Journal of Laser Applications*. 31(2). <https://doi.org/10.2351/1.5096096>
- Bendsøe, MP & Sigmund, O (2003) *Topology Optimization: Theory, Methods, and Applications*. 2nd ed. Berlin: Springer
- Deshpande, VS; Ashby, MF; Fleck, NA. (2001) Foam Topology Bending Versus Stretching Dominated Architectures in *Acta Materialia*. 49(6). [https://doi.org/10.1016/S1359-6454\(00\)00379-7](https://doi.org/10.1016/S1359-6454(00)00379-7)
- Design responses*, viewed 05.05.2021. <https://abaqus-docs.mit.edu/2017/English/SIMACAEANLRefMap/simaanl-c-optdesignresponses.htm>
- Full integration* (2019) in SIMULIA User Assistance. Viewed 13.04.2021. https://help.3ds.com/2019/english/dssimulia_established/simacaegsarefmap/simagsa-c-ctmfull.htm?contextscope=all (URL may require a username and password to access)
- Gay, D; Hua, SV; Tsai, SW. (2003) *Composite Materials: Design and Applications*. CRC Press.
- Hattem, R. n.d. *numpy-stl 2.16.0* viewed 02.03.2021. <https://pypi.org/project/numpy-stl/>
- Holmberg, E; Torstenfelt, B; Klarbring, A. (2014) Fatigue constrained topology optimization in *Struct Multidisc Optim*. 50. <https://doi.org/10.1007/s00158-014-1054-6>
- Kim, H; Lin, Y; Tseng, T-LB. (2018) A review on quality control in additive manufacturing in *Rapid Prototyping Journal*. 24(3). pp. 645-669. <https://doi.org/10.1108/RPJ-03-2017-0048>
- Lee, JW; Yoon, GH; Jeong, SH. (2015) Topology optimization considering fatigue life in the frequency domain in *Computers and Mathematics with Applications*. 70(8). <https://doi.org/10.1016/j.camwa.2015.08.006>
- Liu, YJ; Ren, DC; Li, SJ; Wang, H; Zhang, LC; Sercombe, TB (2020) Enhanced fatigue characteristics of a topology-optimized porous titanium structure produced by selective laser melting in *Additive Manufacturing*. 32. <https://doi.org/10.1016/j.addma.2020.101060>
- Oest, J. (2017) *Structural Optimization with Fatigue Constraints*. PhD Thesis. Aalborg University, Denmark. Available from: https://vbn.aau.dk/files/265255995/PHD_Jacob_Oest_E_pdf.pdf
- Oest, J & Lund, E. (2017) Topology optimization with finite-life fatigue constraints. *Struct Multidisc Optim*. 56. pp. 1045-1059. <https://doi.org/10.1007/s00158-017-1701-9>

- Ozdemir, Z; Hernandez-Nava, E; Tyas, A; Warren, JA; Fay, SD; Goodall, R; Todd, I; Askes, H. (2016) Energy absorption in lattice structures in dynamics: Experiments in *International Journal of Impact Engineering*. 89. pp. 49-61. <https://doi.org/10.1016/j.ijimpeng.2015.10.007>
- Pan, C; Han, Y; Lu, J. (2020) Design and Optimization of Lattice Structures: A Review in *Applied Sciences*. 10(18). <https://doi.org/10.3390/app10186374>
- Pedersen, P. (1989) On optimal orientation of orthotropic materials in *Structural optimization*. 1. pp. 101-106. <https://doi.org/10.1007/BF01637666>
- Sutton M.A. (2008) Digital Image Correlation for Shape and Deformation Measurements. In: Sharpe W. (eds) Springer Handbook of Experimental Solid Mechanics. Springer Handbooks. Springer, Boston, MA. https://doi.org/10.1007/978-0-387-30877-7_20
- Svanberg, K. (1987) The Method of Moving Asymptotes – A New Method for Structural Optimization in *International Journal for Numerical Methods in Engineering*. 24(2). pp. 359-373. <https://doi.org/10.1002/nme.1620240207>
- Tancogne-Dejean, T; Li, X; Diamantopoulou, M; Roth, CC; Mohr, D. (2019) High Strain Rate Response of Additively-Manufactured Plate-Lattices: Experiments and Modeling in *Journal of Dynamic Behavior of Materials*. 5. pp. 361-375. <https://doi.org/10.1007/s40870-019-00219-6>
- Wu, J; Weiming, W; Xifeng, G. (2021) Design and Optimization of Conforming Lattice Structures in *IEEE Transactions on Visualization and Computer Graphics*. 27(1). <https://doi.org/10.1109/TVCG.2019.2938946>
- Zhou, Y & Saitou, K. (2018) Gradient-based multi-component topology optimization for stamped sheet metal assemblies (MTO-S) in *Struct Multidisc Optim*. 58. pp. 83-94. <https://doi.org/10.1007/s00158-017-1878-y>
- Zhu, J; Zhou, H; Wang, C; Zhou, L; Yuan, S; Zhang, W. (2021) A review of topology optimization for additive manufacturing: Status and challenges in *Chinese Journal of Aeronautics*. 34(1). pp. 91-110. <https://doi.org/10.1016/j.cja.2020.09.020>

Appendix

List of figures

Figure 1: Examples of topology optimized and lattice geometry.....	2
Figure 2: Schematic illustration of project workflow.....	3
Figure 3: Effect of SIMP and RAMP interpolation on Young's modulus for a given element fraction ...	6
Figure 4: Element density x_j for SIMP method, penalization factor of 3.	7
Figure 5: Element density x_j for SIMP method, penalization factor of 1.	7
Figure 6: Problem domain.....	10
Figure 7: (Left) shows the basic 2D unit cell, extruded to a 3D shape (Right) is a representation of the 3D elastic properties of the unit cell.....	14
Figure 8: Mohr's circle representation of 2D stress state. (Source: https://commons.wikimedia.org/wiki/File:Mohr_diag17.JPG , accessed 12.04.2021, author Taltastic)	15
Figure 9: Co-projection of stream plot for principal stress fields and density function.	18
Figure 10: Schematic of the lattice generation process	19
Figure 11: CAD geometry and its interpretation by 3D printing slicer software.	20
Figure 12: The three generated lattices.....	21
Figure 13: Tested topology optimized geometries	23
Figure 14: Results from three-point bending experiments on all geometries.	33
Figure 15: Plot of sample stiffness with error bars.....	35
Figure 16: Plot of absolute and specific stiffness.....	37
Figure 17: Absolute and specific load capacity I_c	38
Figure 18: Lattice 2 local buckling failure, without global failure.	40
Figure 19: Absolute and specific work of fracture U	40
Figure 20: Simulation results for RAMP samples.....	41
Figure 21: Simulation results for SIMP samples	42
Figure 22: Simulation results for reference samples.	42
Figure 23: Comparison of simulation results for SIMP and RAMP 70% volume fractions, and the reference geometry	43
Figure 24: Results of convergence analysis on the SIMP 30% volume fraction geometry.	44
Figure 25: DIC (left) and simulation results (right) for principal strain ϵ_{max} for the SIMP 60% volume fraction.....	46
Figure 26: DIC (left) and simulation results (right) for principal strain ϵ_{max} for the SIMP 60% volume fraction at failure	47
Figure 27: Comparison of DIC result with sample failure.	48

Project timeline

Project plan

Activity	Feb	Mar	April	May
Planning				
Creating TopOpt geometry				
Programming, Lat geometry				
Production and testing of samples				
Data analysis				
Literature searches				
Reading				
Learning Abaqus				
Writing				

Time budget

Time budget

Activity	Hours
Planning	15
Administration	10
Learning Abaqus	25
Creating topology optimized geometry	50
Programming lattice generation code	150
Processing and printing samples	10
Testing samples	10
Data analysis	
- DIC	20
- Data entry	5
- Mathematical and regression analysis	30
- Plotting	20
Simulations	30
Literature search	10
Reading	100
Writing	180
SUM	665

